









Tyrosine residues mediate supercontraction in biomimetic spider silk

Gabriele Greco ¹, Tina Arndt ², Benjamin Schmuck², Juanita Francis ², Fredrik G. Bäcklund², Olga Shilkova ², Andreas Barth³, Nathalie Gonska⁴, Gulaim Seisenbaeva ⁵, Vadim Kessler ⁵, Jan Johansson², Nicola M. Pugno ^{1,6}✉ & Anna Rising ^{2,4}✉

Water and humidity severely affect the material properties of spider major ampullate silk, causing the fiber to become plasticized, contract, swell and undergo torsion. Several amino acid residue types have been proposed to be involved in this process, but the complex composition of the native fiber complicates detailed investigations. Here, we observe supercontraction in biomimetically produced artificial spider silk fibers composed of defined proteins. We found experimental evidence that proline is not the sole residue responsible for supercontraction and that tyrosine residues in the amorphous regions of the silk fiber play an important role. Furthermore, we show that the response of artificial silk fibers to humidity can be tuned, which is important for the development of materials for applications in wet environments, eg producing water resistant fibers with maximal strain at break and toughness modulus.

¹Laboratory of Bio-Inspired, Bionic, Nano, Meta, Materials & Mechanics, Department of Civil, Environmental and Mechanical Engineering, University of Trento, Via Mesiano, Trento, Italy. ²Department of Biosciences and Nutrition, Karolinska Institutet, Neo, Huddinge, Sweden. ³Department of Biochemistry and Biophysics, Svante Arrhenius väg 16C, Stockholm University, Stockholm, Sweden. ⁴Department of Anatomy, Physiology and Biochemistry, Swedish University of Agricultural Sciences, Uppsala, Sweden. ⁵Department of Molecular Sciences, Swedish University of Agricultural Sciences, Uppsala, Sweden. ⁶School of Engineering and Materials Science, Queen Mary University of London, Mile End Road, London, UK. ✉email: nicola.pugno@unitn.it; anna.rising@ki.se

Producing large quantities of bioinspired materials is one of the frontiers in science¹ since these can be made from renewable sources and often display properties that out-compete non bioinspired counterparts². Among natural materials, spider silk has attracted much attention during the last few decades^{3–8}. The outstanding mechanical^{9–13} and biological^{14–16} properties of silk have inspired material scientists in the design of biomedical devices and tools with superior properties^{7,17–25}. Examples include sport goods and performance textiles²⁶, components for robotics²⁰, ropes, reinforcements of composite materials, and materials intended for applications in medicine^{18,26}. However, the inherent sensitivity of spider major ampullate silk to humidity poses challenges for several applications²⁷. When exposed to water, the strength and Young's modulus of the fiber decrease, and deformability and toughness modulus increase^{27–30}. Moreover, if the fiber is exposed to wet conditions while unrestrained in both ends, it shrinks in length and twists in a phenomenon known as supercontraction^{24,27,28,31}.

Spider silk proteins (spidroins) consist of two terminal domains with a large internal repetitive region³. The main components of the dragline silk are major ampullate spidroin (MaSp) 1 and 2^{3,32–35}. These two proteins differ mainly in the repetitive region, where GPGXX and di-glutamine motifs can be found in MaSp2 but are missing in MaSp1^{32,34–38}. In the fiber, the repetitive region forms poly-alanine crystalline β -sheets embedded in an amorphous glycine rich matrix^{39–41}. Fourier-transform infrared (FTIR) spectroscopy, X-ray scattering techniques, and nuclear magnetic resonance (NMR) spectroscopy have shown that water entering the fiber affects mainly the amorphous regions, possibly by breaking interchain hydrogen bonds^{8,29,42–47}. However, it is still unclear which amino acid residue types are responsible for the structural changes observed. Proline residues that are abundant in MaSp2 repetitive regions, have been proposed to be important for the contraction and twist of the fibers^{24,48–50}, and possibly also di-glutamine motifs could play a role^{36–38}. Furthermore, molecular dynamics simulations have pointed to the importance of other residues in the repeat region, in particular the side chains of tyrosine and arginine have been predicted to mediate supercontraction⁵¹. Wet lab experimental support for these predictions is difficult to obtain using native silk fibers since they are composed of several different proteins, although some attempts have been made^{52,53}. In this context, heterologous production of spider silk allows design of spidroins with selected amino acid substitutions and an opportunity to investigate supercontraction in fibers made from only one type of protein⁵⁴.

Accordingly, in this work we experimentally investigate supercontraction using a biomimetically produced artificial silk fiber made from the protein NT2RepCT⁵⁵. This protein is void of proline residues in the repetitive region, but this study shows that the fiber still displayed marked supercontraction when exposed to humidity, including the concomitant torsion observed in dragline silk fibers. This suggests that additional residues are involved in the supercontraction and twisting of the fiber. Since tyrosine's OH-group is suggested to be involved in hydrogen bonding with the protein backbone in the dry state but to form hydrogen bonds with bulk water in the wet state and thus could mediate supercontraction⁵¹, we used protein engineering to substitute tyrosine residues in the repeat region with phenylalanine that cannot form hydrogen bonds (NT2Rep^{Y-F}CT) (Fig. 1a). Fibers made from NT2Rep^{Y-F}CT displayed a lower degree of supercontraction and lower susceptibility to humidity, which indicates that also tyrosine residues indeed contribute to supercontraction. Moreover, we show that it is possible to control and tune artificial spider silk supercontraction which will be important for the development of novel silk based materials^{7,19,22,25}.

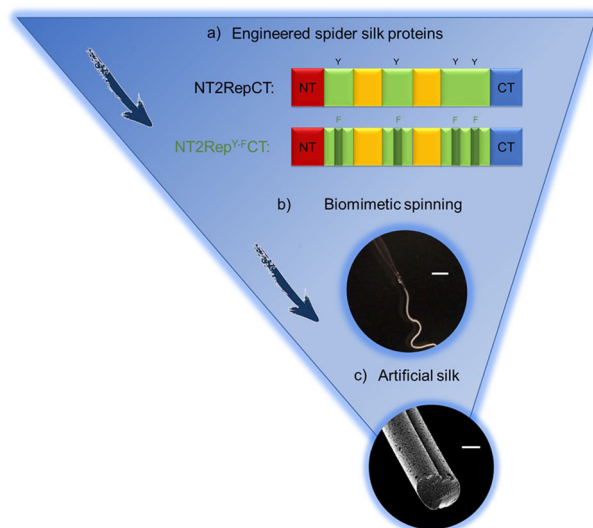


Fig. 1 Schematic presentation of the two designed spider silk proteins used in the study and biomimetic spinning of these into fibers. a The two artificial spider silk proteins studied in this work: NT2RepCT and the NT2Rep^{Y-F}CT. **b** Formation of the biomimetic fibers when entering the spinning bath. Scale bar: 2 mm. **c** FE-SEM picture of the fracture section of the NT2RepCT fiber. Scale bar: 10 μ m.

Results

NT2Rep^{Y-F}CT fibers supercontract less than NT2RepCT fibers.

Artificial spider silk dope made from 300 mg/mL NT2RepCT and NT2Rep^{Y-F}CT (Fig. 1a), respectively, was extruded through a thin glass capillary into a pH 5 aqueous buffer as described previously⁵⁵ (Fig. 1b). Fibers were pulled up from the buffer and collected onto a motorized collection wheel⁵⁶ and dried in air under ambient conditions. To study supercontraction, the fibers were mounted restrained in one end in a humidity chamber. The length and the diameter of ten fibers per type (NT2RepCT and NT2Rep^{Y-F}CT, respectively) were measured before putting the fiber in the chamber and after 2 h at a fixed relative humidity. Both fiber types showed a humidity-induced contraction in length that was positively correlated to relative humidity (Fig. 2 and Supplementary Tables 1 and 2). Notably, at all humidities tested, except at 85%, the NT2Rep^{Y-F}CT fibers showed a significantly lower degree of supercontraction than those made from NT2RepCT. It was also evident that concomitant to the reduction in length there was an increase in diameter for both fiber types (Supplementary Fig. 4). The degree of contraction of both artificial spider silks types was up to 50%, which is similar to what has been observed for native silk⁵². The NT2Rep^{Y-F}CT did not dissolve after being exposed for 2 h to 90% relative humidity, whereas the NT2RepCT did (Supplementary Fig. 5). Thus, supercontraction and susceptibility to dissolution were conspicuously reduced for the NT2Rep^{Y-F}CT fibers.

Artificial spider silk fibers twist during supercontraction.

To observe the sequential events of the supercontraction, we video recorded the fibers when incubated at 85% relative humidity. This revealed that the fibers reacted quickly to the increased humidity and contraction occurred within minutes. Interestingly, we also noted that both NT2RepCT and NT2Rep^{Y-F}CT fibers underwent torsion, in line with what has been previously observed for native silk²⁴ (Supplementary Video 1).

Morphological changes associated with supercontraction. To further investigate the surface topography of the artificial silk

fibers in dry and wet state we used atomic force microscopy (AFM). In the dry state we found that all the fibers presented a relatively smooth surface (Fig. 3a, b). For the NT2RepCT at 75% relative humidity, we noticed an occurrence of bubble-like structures on the surface of the fibers (Fig. 3c, e). In the NT2Rep^{Y-FCT} fibers we did not see any protruding surface structures appearing until 85% relative humidity, at which point a more ripple-like deformation of the surface started to occur (Fig. 3d, f).

Humidity and supercontraction affect the fibers' mechanical properties. The mechanical properties of the NT2RepCT fibers

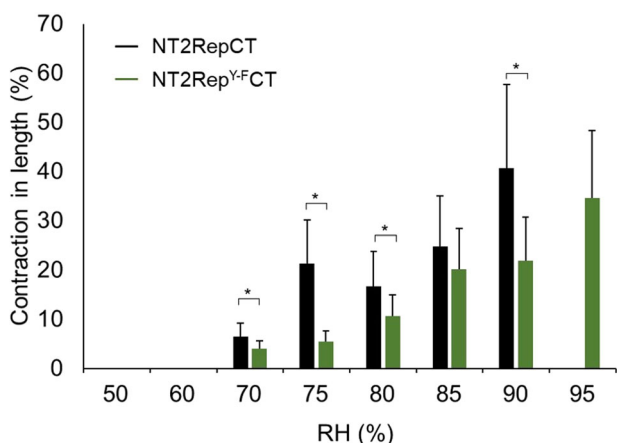


Fig. 2 Supercontraction in response to different relative humidities.

Contraction in length of the fibers when exposed to relative humidity (RH) for 2 h. No contraction was detected at relative humidity < 70% for both the constructs. At 95% the NT2RepCT dissolved, but the NT2Rep^{Y-FCT} did not. Asterisks above the histograms indicate significant differences (p value < 0.05). Black color is used for NT2RepCT fibers and green color for NT2Rep^{Y-FCT} fibers. The error bars are the standard deviation of the data set.

were first tested at different relative humidities. We used a setup where the fibers were incubated for 60 min at a fixed relative humidity with both ends restrained, where mechanical tests were performed while the fiber was still in the chamber (Supplementary Fig. 6a). In this set-up NT2RepCT and NT2Rep^{Y-FCT} fibers displayed similar but not identical responses to different relative humidity in terms of mechanical properties (Fig. 4). Increased humidity resulted in higher strain at break (Fig. 4a), which was most pronounced at >50% relative humidity, and notably at this relative humidity also a yielding point started to appear (start of the plastic region) in the stress strain curves (Supplementary Fig. 6b, c). Strain at break of NT2RepCT fibers correlated with humidity which was not the case for NT2Rep^{Y-FCT} fibers. The strength, on the other hand, did not change with humidity for either of the fiber types (Fig. 4b and Supplementary Fig. 6d) while increased relative humidity resulted in decreased Young's modulus (Fig. 4c and Supplementary Fig. 6e). The toughness modulus showed a tendency to increase with humidity (Fig. 4d and Supplementary Fig. 6f) (which is likely due to the increased deformability) in the case of NT2RepCT fibers while there was no correlation for NT2Rep^{Y-FCT} fibers. The same experimental set-up was also used for native silk, which revealed that natural fibers were less affected by humidity (Supplementary Fig. 9). If the NT2RepCT and NT2Rep^{Y-FCT} fibers were dried after being humidified (restrained at both ends and mounted in the tensile tester), the humidity-induced increase in strain was reversed (Supplementary Fig. 8).

Next, the mechanical properties of the fibers were obtained in the original dried state and after the fibers had been supercontracted (at 85% relative humidity while restrained only at one end) and dried (Fig. 5). Having gone through supercontraction did not affect the strain at break for the NT2RepCT fibers while NT2Rep^{Y-FCT} fibers became less extensible (Fig. 5a and Supplementary Tables 4 and 5). The strength was significantly reduced after supercontraction for both fiber types (Fig. 5b and Supplementary Tables 4 and 5). Consequentially, the toughness modulus was lower for both NT2RepCT and NT2Rep^{Y-FCT} fibers after supercontraction (Fig. 5d and Supplementary Tables 4 and 5). The Young's modulus was not affected in the NT2Rep^{Y-FCT}

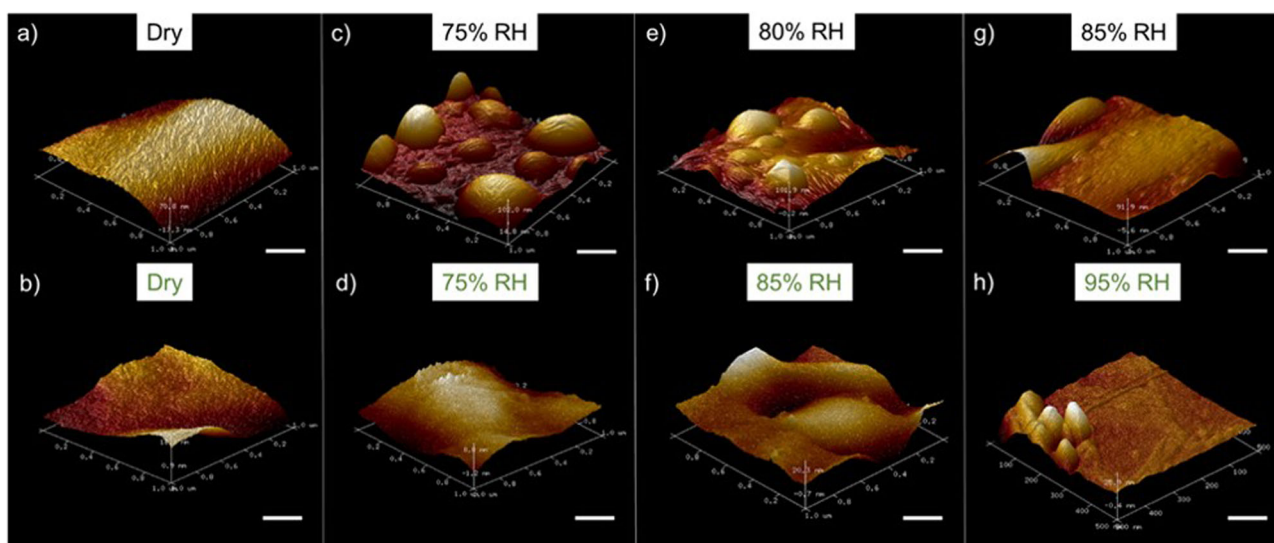


Fig. 3 Atomic force microscopy reveal humidity-induced morphological changes at the fiber surface. Representative AFM images of the NT2RepCT (title in black) and NT2Rep^{Y-FCT} fibers (title in green) in the **a, b** dry state, **c, d** after being supercontracted at 75% relative humidity (RH), **e, f** after being supercontracted at 80% relative humidity. **g** Representative AFM topological image of the NT2Rep^{Y-FCT} fibers contracted at 85% relative humidity and **h** NT2Rep^{Y-FCT} fibers contracted at 95% relative humidity. Scale bars is 100 nm. Black color is used for NT2RepCT fibers and green color for NT2Rep^{Y-FCT} fibers.

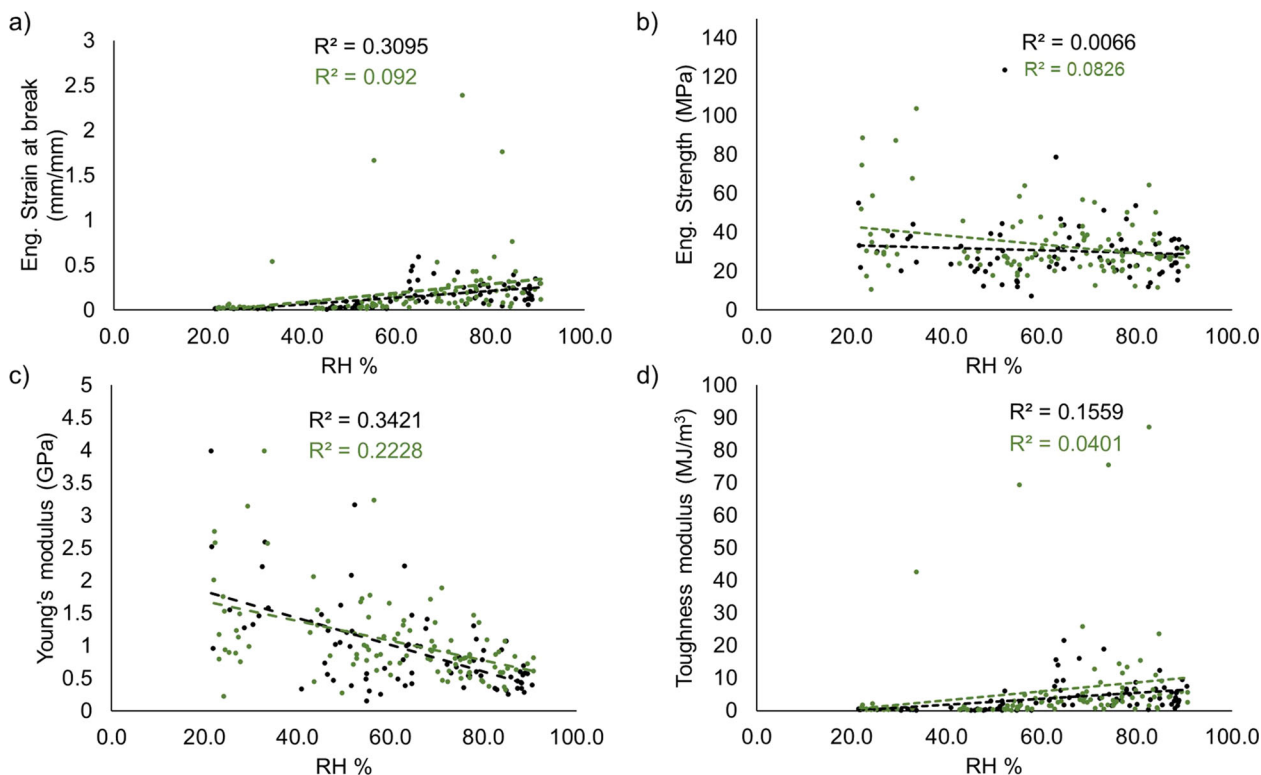


Fig. 4 Fiber mechanical properties at different relative humidity (RH). **a** Eng. Strain at break of the fibers tested at different equilibrium states of relative humidity (RH). **b** Eng. Strength. **c** Young's modulus. **d** Toughness modulus. The color green is used for the NT2Rep^{Y-FCT} and the color black for the NT2RepCT.

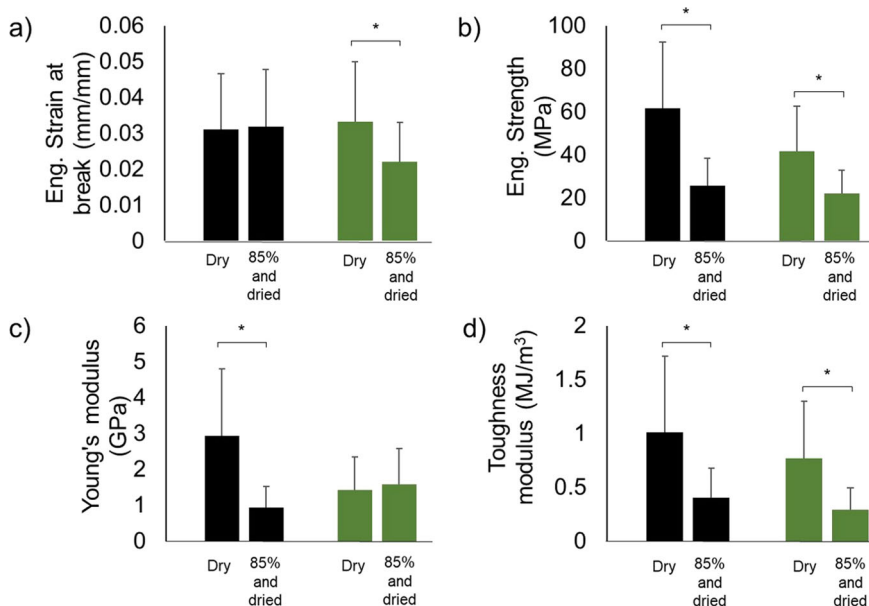


Fig. 5 Mechanical properties of dry and supercontracted fibers. **a** Eng. Strain at break, **b** Eng. Strength, **c** Young's modulus, and **d** toughness modulus of fibers that are as spun (dry) or have been supercontracted at 85% relative humidity while restrained in one end, then dried (at 35% relative humidity) and subsequently tested. Asterisks above the histograms indicate significant differences (p value < 0.05). The color green is used for the NT2Rep^{Y-FCT} and the color black for the NT2RepCT. The error bars are the standard deviation of the data set.

^{FCT} fibers, but it was drastically reduced in the NT2RepCT fibers (Fig. 5c and Supplementary Tables 4 and 5).

Secondary structure content and molecular alignment. To study if the differences in mechanical properties between dry and

supercontracted fibers can be related to differences in the secondary structure content, the fibers were investigated by FTIR spectroscopy (Fig. 6). Here, only very subtle changes in the spectra of both the NT2RepCT and the NT2Rep^{Y-FCT} fiber were found. Thus, the calculated relative distribution of the secondary structure elements suggests a negligible decrease of disordered/ α -

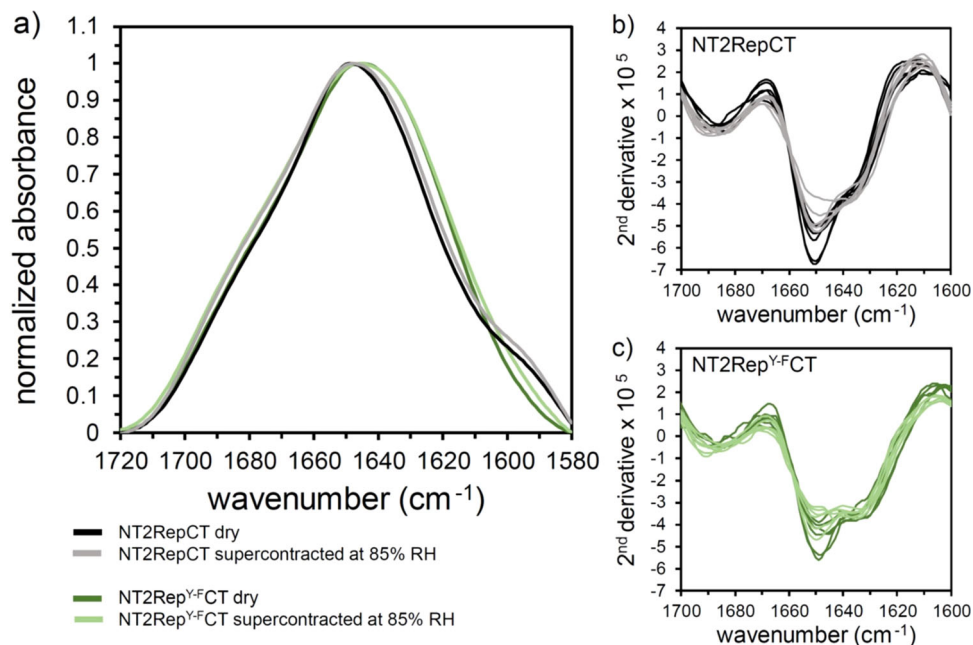


Fig. 6 Secondary structure content analyzed by FTIR spectroscopy. FTIR spectra of NT2RepCT and NT2Rep^{Y-FCT} fibers, measured on dry as spun fibers and fibers that were dried after being supercontracted at 85% relative humidity (RH). **a** Absorbance in the amide I region (1700–1600 cm⁻¹). All spectra represent an average of six measurements, which were baseline subtracted, and normalized. The second derivative of NT2RepCT (**b**) and NT2Rep^{Y-FCT} (**c**), scaled (calculated from the normalized absorbance spectrum and multiplied with a factor 10⁵) and smoothed (Savitzky–Golay window 19 points), from six individual spectra in the amide I region. Black and gray colors are used for NT2RepCT fibers and green colors for NT2Rep^{Y-FCT} fibers.

helical and β -turn elements in supercontracted fibers (Supplementary Table 6). This agrees with the second derivative of the FTIR spectra (Fig. 6b, c), which also suggests a small decrease of disordered/ α -helical (smaller amplitude at 1650 cm⁻¹) relative to the β -sheet content in the supercontracted fibers. However, since the width at half maximal absorbance is increased for the supercontracted fibers relative to the dry fibers (Supplementary Table 7), a more likely interpretation is that the distribution of the secondary structure elements are more heterogenous in the supercontracted fibers⁵⁷.

Polarized microscopy images were captured before and after incubation of both NT2RepCT and NT2Rep^{Y-FCT} fibers at 85% relative humidity in order to investigate if supercontraction causes a significant change in molecular alignment. For both types of fibers, we only detected small and localized changes in birefringence before and after supercontraction (Supplementary Figs. 9–14), thus preventing conclusions on possible changes in the overall molecular organization.

Effects of prolonged incubation in a pH 5 aqueous buffer. To investigate the possibility of using our artificial fibers in wet environments, we tested their susceptibility to water or phosphate buffered saline (PBS) and found that both NT2Rep^{Y-FCT} and NT2RepCT fibers dissolved when submerged. As increased incubation times in low pH aqueous buffers can improve mechanical properties and lead to more water resistant fibers⁵⁶, we prolonged the incubation time in the spinning bath. In line with previously published results for NT2RepCT fibers, NT2Rep^{Y-FCT} fibers that had been incubated for >3 h in the spinning bath and dried remained intact after submersion in water and PBS, respectively, (Supplementary Fig. 15). We also observed an increase in strain at break for the NT2Rep^{Y-FCT} fibers during the first 5 h of incubation which was reversed after 24 and 48 h incubation (Supplementary Fig. 15a). The strength

and the Young's modulus were not affected by prolonged incubation (Supplementary Fig. 15b, c), which is also in line with previous observations for NT2RepCT fibers⁵⁶. The toughness modulus increased for the first 5 h of incubation and then decreased thereafter (Supplementary Fig. 15d). This shows that incubation time can be optimized for maximizing both ductility and toughness. Future work should investigate supercontraction after immersion of the fibers in water, which would allow determination of the α parameter⁵⁸.

Discussion

Understanding supercontraction in native spider silk fibers and controlling this phenomenon in artificial replicas are crucial for developing this material for applications in humid/wet environments. Despite this, relatively little is known about the molecular events that cause the humidity-induced contraction, torsion, and swelling of the native fiber. This is likely due to the fact that native silks are composed of a mixture of different proteins and hence the molecular details of supercontraction are difficult to study^{8,51}. In this context, our artificial spider silk fibers offer a system where this phenomenon can be studied experimentally since the fibers are composed of one type of protein only, and the heterologous production mode makes protein engineering feasible and effects of individual amino acid residues can thus be studied. Here we show that artificial spider silk fibers made from the NT2RepCT protein display the classical hallmarks of supercontraction in native silks, which include humidity-induced torsion²⁴, contraction⁵², and increased plasticity⁵⁹. Although supercontraction has previously been observed for artificial spider silk⁶⁰, quantitative data of the phenomenon was obtained solely by molecular dynamics simulations, and the values presented differed from the experimentally determined ones of the native material⁵². The rationale for using the NT2RepCT protein in this study is that it is the first reported recombinant silk protein that

can be spun into fibers using a biomimetic spinning process that recapitulates important molecular events associated with natural spider silk spinning^{55,61,62}, and thereby represents a more relevant model for studying changes in protein conformation compared to fibers that require denaturing agents and coagulation baths for production.

Molecular dynamics simulation studies of repetitive domains and studies using X-ray diffraction, and NMR and FTIR spectroscopy on native silk fibers show that it is mainly the glycine rich amorphous regions of the fiber that are affected when the fiber supercontracts^{29,42–48,51,63–67}. Water molecules are suggested to enter the fiber, breaking interchain hydrogen bonds that cause the amorphous regions to contract^{45,47,68,69}. Proline residues are often suggested to be the crucial mediator of supercontraction^{49,50} based on that spider silks with higher proline content supercontract more⁴⁹. However, the repetitive region of NT2RepCT is derived from a MaSp1 protein and is thus void of proline residues, still the NT2RepCT fibers supercontract in response to increased humidity, even to a similar degree as natural spider silk (Fig. 2)⁵². Recently, Giesa et al.⁵¹ performed a molecular dynamics simulation study on repetitive segments where they showed that tyrosine residues in the amorphous region are involved in supercontraction. Based on this, we engineered a NT2Rep^{Y-FCT} of NT2RepCT in which the tyrosine residues were substituted with phenylalanines (NT2Rep^{Y-FCT}). Phenylalanine side chain, in contrast to tyrosine, lacks the hydroxyl group that is proposed to be involved in hydrogen bonding^{70,71}, hence the NT2Rep^{Y-FCT} fibers are expected to be more resistant to humidity. Indeed, the NT2Rep^{Y-FCT} fibers contracted less than NT2RepCT fibers when exposed to different humidity rates (Fig. 2). Moreover, the NT2Rep^{Y-FCT} fibers did not dissolve when exposed to high humidity conditions (relative humidity >90%). This shows that tyrosine residues in the repetitive region of NT2RepCT fibers are involved in supercontraction, but additional factors, e.g. like the influence of the terminal domains and effect of other primary structure features as well as the impact of varying length of the repetitive part, remain to be determined.

To investigate the impact of increased humidity on fiber surface topography, we used AFM microscopy of fibers that had been incubated at different relative humidity (Fig. 3). At relative humidity higher than 75% (when supercontraction starts) we observed the appearance of bubble-like structures on the surface of NT2RepCT fibers (Fig. 3b). Such bubble-like structures have previously been suggested to be related to the dissolution process of native silk⁷². In contrast, the NT2Rep^{Y-FCT} fibers did not present the bubble-like structures until 85% of relative humidity and the structures appearing then were more ripple-like (Fig. 3d, f). This is in accordance with the increased resistance to humidity-induced supercontraction we observed for the NT2Rep^{Y-FCT} fibers (Fig. 2).

Recently, spider silk fibers were shown not only to contract but also to undergo a twist when exposed to humidity²⁴. Molecular dynamics simulations have pointed towards proline residues being responsible for this phenomenon²⁴. To our surprise, this phenomenon (torsion, Supplementary Video 1) is recapitulated by NT2RepCT and NT2Rep^{Y-FCT} fibers which indicates that additional residues and/or molecular events that are yet to be identified are involved. In line with the notion that proline is not the sole mediator of the twisting behavior, the degree of torsion observed in Liu et al.²⁴ differed in two silk fibers that were expected to have similar proline contents⁴⁹.

Exposure of silk fibers to water also affects the mechanical properties of both native and artificial spider silk. Here, we report the effects of different relative humidity on mechanical properties of artificial spider silk. The first aspect that we noticed is the occurrence of the yielding point at humidity rates higher than

60% (Supplementary Fig. 6b). In this context, Keten et al.⁴⁰ proposed a nanomechanical model of silk in which the response to traction of the fiber is due to the gradual load transfer from the amorphous domains to the crystalline ones. The yielding point occurs when the hydrogen bonds break in the amorphous domains, leading to their unfolding and thus providing deformability to the fiber. Thus, a humidity-induced higher disorder in the amorphous region (higher capability in unfolding) can lead to the observed occurrence of the yielding point and thus higher deformability⁵⁰, which is in accordance with our results from NT2RepCT fibers (Fig. 4a).

Since restraining the silk fiber affects its response to humidity^{18,73}, we investigated the mechanical properties of fibers that were supercontracted at 85% with only one end restrained and then dried (Fig. 5 and Supplementary Table 1). In general, fibers supercontracted in this way presented poorer mechanical performances with respect to the original dry ones, which is an important aspect to take into consideration for applications where cyclic exposure to different relative humidities is needed, e.g., chemical sensors^{22,25}. To investigate if differences in secondary structure content could reveal the mechanisms behind the altered mechanical properties of supercontracted fibers, they were analyzed by FTIR spectroscopy. However, we could not find any significant changes of the relative distribution of secondary structures, but the data indicate a more heterogenous distribution of the secondary structure elements (Fig. 6 and Supplementary Tables 2 and 3), which agrees with previous studies using wide angle x-ray scattering on native silk²⁹.

In summary, we show that biomimetically spun NT2RepCT fibers recapitulate the humidity-induced supercontraction and twisting behavior of natural spider silk fibers. This is surprising considering that the repetitive region of NT2RepCT is void of proline residues and indicates that additional residues and/or structural events are involved in these processes. Furthermore, we present experimental evidence of the involvement of tyrosine residues in supercontraction and show that tuning the supercontraction behavior of artificial spider silk is possible by rational protein engineering. This will be important for the development of artificial silk fibers that have defined responses to different relative humidity, e.g., for motional control or for making adaptable wearables¹⁸. Other applications may require the material to be completely resistant to wet and humid environments, why future studies should be targeted at experimentally dissecting the molecular events of supercontraction and at the engineering of such fibers.

Conclusions

In this work, we present a system for detailed analysis of the supercontraction phenomenon of artificial spider silk fibers. Results show that tyrosine residues, but not necessarily proline residues, in the repetitive domain affect humidity-induced changes of the fibers. Torsion was observed also in fibers void of proline residues in the repetitive region suggesting that additional residues are involved in this phenomenon. Finally, we show that supercontraction of biomimetic artificial spider silk can be tuned by rational protein engineering. This approach is important for improving our basic understanding of the supercontraction phenomenon as well as for the production of advanced bioinspired engineered materials.

Methods

Preparation of the spinning dope. The primary structure of NT2RepCT and NT2Rep^{Y-FCT} is found in Supplementary Fig. 1. The difference between the two proteins is found in the repetitive region, which contains 5% of tyrosine in NT2RepCT (corresponding to the wild type sequence) and, instead, 5% of phenylalanine in NT2Rep^{Y-FCT}. NT2RepCT and the NT2Rep^{Y-FCT} proteins were

expressed and purified essentially as described before⁵⁵. Briefly, an overnight (ON) culture (30 °C and 200 rpm) was prepared by inoculating Luria broth (LB) media containing kanamycin (70 µg/L) with *Escherichia coli* BL21 (DE3) harboring the plasmid pT7-6xHis-NT2RepCT. The ON culture was diluted 100 times into 1 L of fresh LB media with kanamycin (70 µg/L) and cultured at 30 °C with shaking (110 rpm). Once the OD₆₀₀ reached 0.6, the temperature was reduced to 20 °C until OD₆₀₀ reached 0.8–0.9. Expression was induced by adding isopropylthiogalactoside to a final concentration of 0.3 mM. Cells were harvested 20 h after induction by centrifugation, at 7278 × *g* for 20 min. The cell pellet was resuspended in 20 mM Tris-HCl (pH 8) and frozen at –20 °C. Thawed cells were lysed using a cell disruptor (T-series Machine, Constant Systems Limited, Daventry, Northants, UK) at 30 kPsi and 4 °C. The lysate was centrifuged at 27,000 × *g* at 4 °C for 30 min. Purification was performed using the Ni-NTA column protocol as described earlier⁵⁵. However, after loading the supernatants, two wash steps were conducted: one containing 20 mM Tris-HCl (pH 8) and a second wash additionally containing 5 mM imidazole. The protein was eluted with 300 mM imidazole in 20 mM Tris-HCl (pH 8) and dialyzed against an excess amount of 20 mM Tris-HCl (pH 8) to remove the imidazole. The protein was concentrated to ~300 mg/mL as described previously³⁹ using an ultrafiltration spin column (Vivaspin 20, GE Healthcare, Chicago, IL, USA). The protein concentrations were calculated using the molar extinction coefficient of NT2RepCT (18910 M⁻¹cm⁻¹) and NT2Rep^{Y-FCT} (12950 M⁻¹cm⁻¹), respectively. The protein dopes were transferred into 1 mL syringes with Luer Lok tip (BD, Franklin Lakes, NJ, USA) and frozen at –20 °C.

Artificial spider silk spinning. Fiber spinning was performed following Andersson et al.⁵⁵ and the fibers were collected onto a motorized wheel in air as described in Greco et al.⁵⁶ Briefly, syringes containing concentrated protein dope were thawed and connected to a needle with an outer diameter (O.D.) of 0.40 mm (blunt end steel, B. Braun, Germany) and two polyethylene tubing both ~20 mm in length. The first tubing had an O.D. of 1.09 mm and an inner diameter (I.D.) of 0.38 mm and the second tubing had an O.D. of 1.65 and I.D. of 0.67 (BD Intramedic, USA). Round glass capillary with an O.D. of 1.00 mm and an I.D. (G1 Narishige, Japan) were pulled with a Micro Electrode Puller (Stoelting Co., USA) and cut to a O.D. of 25–35 µm. A capillary was connected to the tubing and the set-up was fitted in an neMESYS low pressure (290 N) syringe pump (Cetoni, Germany) to extrude the protein with a flow-rate of 17 µl/min into a spinning bath (500 mM NaAc and 200 mM NaCl, pH 5). Fibers were collected 30 cm from the tip of the capillary on six diapositive slide frames mounted on a motorized wheel (diameter 11.5 cm) without stretching the fibers. For investigations of the impact of prolonged incubation in the spinning buffer on mechanical properties, we collected the fibers onto a circular roller with a diameter of 30 mm, submerged into the spinning buffer⁵⁶. The roller was placed ~30 cm from the tip of the capillary and rotated counterclockwise. Extruding fibers were guided along the collection bath using a 1 µL inoculation loop and picked up by the roller. After spinning, fibers were either removed immediately from the roller or were kept on the submerged roller in the spinning buffer for 3, 5, 5.5, 6, 24, and 48 h, respectively. Fibers were removed from the roller using surgical tweezers at each incubation time and placed on a black plastic sheet to dry.

Native spider silk. *Trichonephila clavipes* spiders were used to investigate the effect of humidity on the mechanical properties of native silk fibers. The silk from this species serves as a good control for studying changes in mechanical properties in response to humidity, but it should be noted that it does not supercontract to a large extent, i.e., its maximal contraction is around 20% compared to 45% for *Araneus diadematus* major ampullate silk⁵². From whole webs we collected the supporting threads that are produced mainly by the major ampullate gland⁷⁴. The spider was watered and fed weekly. The silk samples were mounted with a slack on paper frames. This was done to avoid humidity-induced fiber tension that would affect the mechanical properties.

Tensile tests. The fibers were mounted on a 1 cm square window cut in a paper frame as performed in previous studies⁷⁴, and fixed using a double sided tape. For tensile tests, a 5943-Instron tensile tester with a 5 N load cell was used. The machine was calibrated by measuring the mechanical properties of standard commercial fibers (Teijin Technora T240-440dtext®, SGL C T24-5.0/270-E100®) as well as natural spider silk (*Trichonephila clavipes*) and by using weights. The displacement speed was 6 mm/min, which is in accordance to previously used protocols^{9,10,14,17,56,74–77}, but it should be noted that this relatively fast extension rate could result in enhanced properties compared to protocols that use a slower extension rate^{9,11,29,78,79}. The machine measures the load and the displacement; we thus computed the engineering stress (σ) by dividing the measured force (F) by the cross-sectional area (A) of each tested fiber (the Eng. Strength was taken as the failure Eng. Stress). In math

$$\sigma = \frac{F}{A} \quad (1)$$

The fiber diameter used in the calculations was a mean value of five measurements at arbitrary positions along the fiber, measured by an optical microscope⁷⁵. The cross-section of the fibers was assumed to be circular, but as reported previously⁵⁶, the fibers show a dumbbell shaped cross-section

(Fig. 1c). This means that in the optical microscope the largest possible diameter is obtained, and when assuming a circular cross section, the area is overestimated and, consequently, the stress is underestimated. The engineering strain (ϵ) was computed by dividing the displacement (ΔL) by the gauge length (L_0); in math

$$\epsilon = \frac{\Delta L}{L_0} \quad (2)$$

The Young's modulus was computed by the slope of the Eng. Stress – Eng. Strain curve in the initial linear elastic part. The toughness modulus was obtained by measuring the area under the Eng. Stress – Eng. Strain curve. For the humidity tests, the single fibers were kept in the tensile tester at a fixed relative humidity for at least 60 min prior to testing. The samples mounted were prepared with a slack to avoid the generation of tension due to humidity-induced contraction. For all tests, the temperature was between 19 and 21 °C.

Statistical analysis. Analysis of the variance was performed to compare the mechanical and morphological properties of different sets of dry and supercontracted fibers. The parameters used to verify the null hypothesis, i.e., all the data sets come from the same distribution and have the same mean value, were

$$SSQ_a = \sum_{g=1}^G n_g (m_g - m)^2 \quad (3)$$

$$SSQ_e = \sum_{g=1}^G \sum_{j=1}^{n_g} (x_{gj} - m_g)^2 \quad (4)$$

where G is the number of different samples under consideration, n_g is the number of tests of the same sample, m is the mean value of all the data, m_g is the mean value within the group (i.e., sample), and x is the single value. These sums of squares were used to compute the T value, namely

$$T = \frac{SSQ_a}{\frac{G-1}{SSQ_e}} \quad (5)$$

that has been compared with the ideal value of the Fisher function F . If $T > F$ we reject the null hypothesis and thus we can consider the difference among the data set as significant. This parameter and the two tailed p value were computed with Matlab®. Significance was assigned for p values lower than 5% ($p < 0.05$).

We also performed MANOVA analysis, since there are multiple response variables (i.e., Eng. Strain at break, Eng. Strength, Young's modulus, and toughness modulus). Thus, we were interested in determining whether the entire set of means is different from one group to the next. The grouping variable was the treatment on the fibers (e.g., supercontracted at 85% and then dried). The p values of the group means were computed by means of Matlab®, following Adachi⁸⁰.

Humidity chamber. The humidity chamber was built using a polystyrene foam box adapted to the tensile tester (parts were carved out to make the box fit the tensile tester). A digital hygrometer sensor connected to a remote display was inserted in the box which allowed monitoring of the relative humidity. The humidity was set by putting a wet cloth inside the chamber. The stability of the humidity was tested several times for different durations, namely 1, 2, and 24 h to ensure functionality (Supplementary Fig. 2).

Supercontraction measurements. To measure the supercontraction at different relative humidity, fibers were mounted with one end restrained and exposed to a specific relative humidity (%) for 2 h in the humidity chamber at 60, 70, 75, 80, 85, 90, and 95%. The diameter of the fibers was measured prior and after the treatment, at 50 locations per fiber by an optical light microscope (Nikon eclipse TE300). Assuming that the probability distribution of the diameter is Gaussian, we compared the probability distribution before and after the exposure to humidity through ANOVA (Supplementary Fig. 3). The length of the fibers (placed on black paper) was measured with a caliper before and after the test. For each set of fibers (ten fibers per set) the change in length and diameter as well as the mean value and the standard deviations thereof were calculated. Additionally, mechanical properties of fibers supercontracted at 85% relative humidity were measured. For the video recordings (to qualitatively observe supercontraction), fibers were mounted on paper frames and monitored with a Canon EOS 700D.

Dissolution experiments. This procedure was done for the NT2Rep^{Y-FCT} fibers as described in Greco et al.⁵⁶. Briefly, fibers were incubated in spinning buffer for various times scales (3, 5, 5.5, 6, 24, and 48 h), dried and placed in dH₂O and 1 x PBS, respectively, and their integrity was observed by the naked eye after 24 h, 48 h, and 1 week.

Scanning electron microscopy (SEM). A FESEM Zeiss–40 Supra microscope was used to analyze the surface structure of the fibers. The metallization was performed using a sputtering instrument (Quorum Q150T) with a sputtering mode of Pt/Pd 80:20 for 5 min.

Atomic force microscopy (AFM). After being kept at the desired relative humidity conditions for at least 2 h, the fibers were dried (assuming that supercontraction is irreversible^{81,82}), placed on double sided tape, mounted on a quartz support, and kept in a controlled environment for 1 week (35% relative humidity and 20 °C). To investigate the morphology of the fibers we used pre-calibrated Bruker's tip: FASTSCAN-B Silicon Tip on Silicon Nitride Cantilever with a backside coating of Au in a Bruker FastScan Bio™ Atomic Force Microscope. The nominal length of the tip was 30 μm, the thickness 0.3 μm, its resonance frequency 400 kHz, the width 32 μm and the spring constant 4 N/m. The used analysis software was Nanoscope Analysis 1.9. The images were obtained with a tapping mode scan, with the rate of 3.07 Hz and 512 lines (1 μm²).

Fourier-transform infrared (FTIR) spectroscopy. For FTIR spectroscopy a Vertex 70 instrument was used, equipped with a diamond crystal (Platinum-ATR, Bruker) and a mercury cadmium telluride (MCT) detector (Bruker). The spectra were obtained on fibril bundles in triplicate both parallel and perpendicular to the beam. For each fiber 200 scans were performed with a resolution of 2 cm⁻¹. The absorbance spectra for each fiber were averaged, and baseline subtracted using a second-degree polynomial baseline type between 1740, 1730, 1580, and 1578 cm⁻¹. Then the amide I region (1700–1600 cm⁻¹) was fitted with the software Kinetics by E. Goormaghtigh (Université Libre de Bruxelles, Belgium). To compute the secondary structure content of the fibers, a procedure described earlier was used^{83,84}. Briefly, the absorbance and the second derivative were simultaneously co-fitted using eight component bands. The absorbance spectra were smoothed with a Savitzky–Golay window of 13, 15, 17, and 19 points (resulting in four differently smoothed spectra) and the second derivatives were scaled with a weighting factor of 300. At ~1696, ~1637, ~1625, and ~1614 cm⁻¹ the component bands were assigned to β-sheets. The wavenumber at ~1654 cm⁻¹ represented the component band for α-helix/random structures, and at ~1672 cm⁻¹ turns were assigned. The secondary structure contents obtained with the four fits were averaged for each fiber type, which yielded the final relative distribution of the secondary structure elements.

Polarized light microscopy. Polarized light images were acquired using a Nikon Eclipse Ts2R-FL microscope equipped with polarizers and a DFK 33UX264 (2448 × 2048, 5 MP) color camera. All polarized light images were acquired using the same settings. A sample fiber was secured at one end with a tape attached to a paper frame, which was placed on a microscope glass slide for imaging. Three sequential non overlapping images were acquired, starting from the end of the fiber located closer to the tape. This was done for each of three NT2RepCT as well as NT2Rep^Y-FCT fibers before and after incubation at 85% relative humidity in a humidity chamber for 2 h.

Data availability

All data generated or analyzed during this study are included in this published article (and its supplementary information files).

Received: 9 December 2020; Accepted: 8 March 2021;

Published online: 12 April 2021

References

- Wegst, U. G. K., Bai, H., Saiz, E., Tomsia, A. P. & Ritchie, R. O. Bioinspired structural materials. *Nat. Mater.* **14**, 23–36 (2015).
- Vincent, J. F. V., Bogatyreva, O. A., Bogatyrev, N. R., Bowyer, A. & Pahl, A. K. Biomimetics: its practice and theory. *J. R. Soc. Interface* **3**, 471–482 (2006).
- Eisoldt, L., Smith, A. & Scheibel, T. Decoding the secrets of spider silk. *Mater. Today* **14**, 80–86 (2011).
- Asakura, T. & Miller, T. *Biotechnology of Silk*. (Springer, 2014).
- Basu, A. *Advances in Silk Science and Technology*. (The Textile Institute, 2015).
- Vepari, C. & Kaplan, D. L. Silk as a biomaterial. *Prog. Polym. Sci.* **32**, 991–1007 (2007).
- Salehi, S., Koeck, K. & Scheibel, T. Spider silk for tissue engineering applications. *Molecules* **25**, 737 (2020).
- Vollrath, F. & Knight, D. P. Liquid crystal spinning of spider silk. *Nature* **410**, 541–548 (2001).
- Greco, G. & Pugno, N. M. Mechanical properties and Weibull Scaling Laws of unknown spider silks. *Molecules* **25**, 2938 (2020).
- Greco, G., Wolff, J. & Pugno, N. M. Strong and tough silk for resilient attachment discs: the mechanical properties of piriform silk, in the spider *Cupiennius salei* (Keyserling, 1877). *Front. Mater.* **7**, <https://doi.org/10.3389/fmats.2020.00138> (2020).
- Agnarsson, I., Kuntner, M. & Blackledge, T. A. Bioprospecting finds the toughest biological material: extraordinary silk from a giant riverine orb spider. *PLoS ONE* **5**, 1–8 (2010).
- Porter, D., Guan, J. & Vollrath, F. Spider silk: super material or thin fibre? *Adv. Mater.* **25**, 1275–1279 (2013).
- Gosline, J. et al. Elastic proteins: biological roles and mechanical properties. *Philos. Trans. R. Soc. B Biol. Sci.* **357**, 121–132 (2002).
- Yang, Y. et al. Spider (*Linothele megatheloides*) and silkworm (*Bombyx mori*) silks: comparative physical and biological evaluation. *Mater. Sci. Eng. C* **107**, 110197 (2020).
- Kuhbier, J. W. et al. Interactions between spider silk and cells - NIH/3T3 fibroblasts seeded on miniature weaving frames. *PLoS ONE* **5**, 1–9 (2010).
- Allmeling, C., Jokuszies, A., Reimers, K., Kall, S. & Vogt, P. M. Use of spider silk fibres as an innovative material in a biocompatible artificial nerve conduit. *J. Cell. Mol. Med.* **10**, 770–777 (2006).
- Dellaquila, A. et al. Optimized production of a high-performance hybrid biomaterial: biomimetic spider silk for bone tissue engineering. *J. Appl. Polym. Sci.* **48739**, 1–9 (2019).
- Agnarsson, I., Dhinojwala, A., Sahni, V. & Blackledge, T. A. Spider silk as a novel high performance biomimetic muscle driven by humidity. *J. Exp. Biol.* **212**, 1990–1994 (2009).
- Altman, G. H. et al. Silk-based biomaterials. *Biomaterials* **24**, 401–416 (2003).
- Pan, L. et al. A supertough electro-tendon based on spider silk composites. *Nat. Commun.* **11**, 1332 (2020).
- Yuan, A. Y., Yu, Q., Wen, J., Li, C. & Guo, Z. Ultrafast and highly selective uranium extraction from seawater by hydrogel-like spidroin-based protein fiber. *Angew. Chem. Int. Ed.* <https://doi.org/10.1002/anie.201906191> (2019).
- Hey Tow, K. et al. Exploring the use of native spider silk as an optical fibre for chemical sensing. *J. Light. Technol.* **8724**, 1–8 (2017).
- Steven, E. et al. Carbon nanotubes on a spider silk scaffold. *Nat. Commun.* **4**, 1–8 (2013).
- Liu, D. et al. Spider dragline silk as torsional actuator driven by humidity. *Sci. Adv.* **5**, eaau9183 (2019).
- Hey Tow, K. et al. Spider silk: a novel optical fibre for biochemical sensing. *Proc. of SPIE* **9634**, 96347D (2015).
- Bourzac, K. Spiders: a web of intrigue. *Nature* **519**, S4–S6 (2015).
- Elices, M., Plaza, G. R., Pérez-Rigueiro, J. & Guinea, G. V. The hidden link between supercontraction and mechanical behavior of spider silks. *J. Mech. Behav. Biomed. Mater.* **4**, 658–669 (2011).
- Liu, Y., Shao, Z. & Vollrath, F. Relationships between supercontraction and mechanical properties of spider silk. *Nat. Mater.* **4**, 901–905 (2005).
- Yazawa, K., Malay, A. D., Masunaga, H., Norma-Rashid, Y. & Numata, K. Simultaneous effect of strain rate and humidity on the structure and mechanical behavior of spider silk. *Commun. Mater.* **1**, 10 (2020).
- Cohen, N., Levin, M. & Eisenbach, C. D. On the origin of supercontraction in spider silk. *Biomacromolecules*. <https://doi.org/10.1021/acs.biomac.0c01747> (2021).
- Work, R. W. Dimensions, birefringences, and force-elongation behavior of major and minor ampullate silk fibers from orb-web-spinning spiders—The effects of wetting on these properties. *Text. Res. J.* **47**, 650–662 (1977).
- Hinman, M. B. & Lewis, V. Isolation of a clone encoding a second dragline silk fibroin. *Nephila clavipes* dragline silk is a two-protein fiber. *J. Biol. Chem.* **267**, 19320–19324 (1992).
- Xu, M. & Lewis, R. V. Structure of a protein superfiber: spider dragline silk. *Proc. Natl Acad. Sci. USA* **87**, 7120–7124 (1990).
- Motriuk-smith, D., Smith, A., Hayashi, C. Y. & Lewis, R. V. Analysis of the conserved N-terminal domains in major ampullate spider silk proteins. *Biomacromolecules* **6**, 3152–3159 (2005).
- Sponner, A. et al. Characterization of the protein components of *Nephila clavipes* dragline silk. *Biochemistry* **44**, 4727–4736 (2005).
- Malay, A. D., Arakawa, K. & Numata, K. Analysis of repetitive amino acid motifs reveals the essential features of spider dragline silk proteins. *PLoS ONE* **12**, 1–16 (2017).
- Rising, A. et al. Major ampullate spidroins from *Euprosthenops australis*: multiplicity at protein, mRNA and gene levels. *Insect Mol. Biol.* **16**, 551–561 (2007).
- Hayashi, C. Y. & Lewis, R. V. Evidence from flagelliform silk cDNA for the structural basis of elasticity and modular nature of spider silks. *J. Mol. Biol.* **275**, 773–784 (1998).
- Savage, K. N. & Gosline, J. M. The effect of proline on the network structure of major ampullate silks as inferred from their mechanical and optical properties. *J. Exp. Biol.* **211**, 1937–1947 (2008).
- Keten, S., Xu, Z., Ihle, B. & Buehler, M. J. Nanoconfinement controls stiffness, strength and mechanical toughness of B-sheet crystals in silk. *Nat. Mater.* **9**, 359–367 (2010).
- Hijirida, D. H. et al. 13C NMR of *Nephila clavipes* major ampullate silk gland. *Biophys. J.* **71**, 3442–3447 (1996).
- Work, R. W. Viscoelastic behaviour and wet supercontraction of major ampullate silk fibres of certain orb-web-building spiders (Araneae). *J. Exp. Biol.* **118**, 379LP–404LP (1985).

43. Parkhe, A. D., Seeley, S. K., Gardner, K., Thompson, L. & Lewis, R. V. Structural studies of spider silk proteins in the fiber. *J. Mol. Recognit.* **10**, 1–6 (1997).
44. Bonthrone, K. M., Vollrath, F., Hunter, B. K. & Sanders, J. K. M. The elasticity of spiders' webs is due to water-induced mobility at a molecular level. *Proc. R. Soc. Lond. B* **248**, 141–144 (1992).
45. Holland, G. P., Lewis, R. V. & Yarger, J. L. WISE NMR characterization of nanoscale heterogeneity and mobility in supercontracted *Nephila clavipes* spider dragline silk. *J. Am. Chem. Soc.* **126**, 5867–5872 (2004).
46. Ene, R., Papadopoulos, P. & Kremer, F. Supercontraction in *Nephila* spider dragline silk - Relaxation into equilibrium state. *Polymer*. **52**, 6056–6060 (2011).
47. Eles, P. T. & Michal, C. A. Strain dependent local phase transitions observed during controlled supercontraction reveal mechanisms in spider silk. *Macromolecules* **37**, 1342–1345 (2004).
48. Shi, X., Yarger, J. L. & Holland, G. P. Elucidating proline dynamics in spider dragline silk fibre using ^2H - ^{13}C HETCOR MAS NMR. *Chem. Commun.* **50**, 4856–4859 (2014).
49. Liu, Y., Spohner, A., Porter, D. & Vollrath, F. Proline and processing of spider silks. *Biomacromolecules* **9**, 116–121 (2008).
50. Savage, K. N. & Gosline, J. M. The role of proline in the elastic mechanism of hydrated spider silks. *J. Exp. Biol.* **211**, 1948–1957 (2008).
51. Giesa, T., Schuetz, R., Fratzl, P., Buehler, M. J. & Masic, A. Unraveling the molecular requirements for macroscopic silk supercontraction. *ACS Nano* **11**, 9750–9758 (2017).
52. Boutry, C. & Blackledge, T. A. Evolution of supercontraction in spider silk: structure-function relationship from tarantulas to orb-weavers. *J. Exp. Biol.* **213**, 3505–3514 (2010).
53. Blamires, S. J., Wu, C.-L., Blackledge, T. A. & Tso, I.-M. Post-secretion processing influences spider silk performance. *J. R. Soc. Interface* **9**, 2479–2487 (2012).
54. Johansson, J. & Rising, A. Doing what spiders cannot - A road map to supreme artificial silk fibers. *ACS Nano* **15**, 1952–1959 (2021).
55. Andersson, M. et al. Biomimetic spinning of artificial spider silk from a chimeric minispidroin. *Nat. Chem. Biol.* **13**, 262–264 (2017).
56. Greco, G. et al. Properties of biomimetic artificial spider silk fibers tuned by postSpin bath incubation. *Molecules* **25**, 3248 (2020).
57. Barth, A. Infrared spectroscopy of proteins. *Biochim. Biophys. Acta* **1767**, 1073–1101 (2007).
58. Madurga, R. et al. Material properties of evolutionary diverse spider silks described by variation in a single structural parameter. *Sci. Rep.* **6**, 1–8 (2016).
59. Vollrath, F. & Edmonds, D. T. Modulation of the mechanical properties of spider silk by coating with water. *Nature* **340**, 305–307 (1989).
60. Venkatesan, H. et al. Artificial spider silk is smart like natural one: having humidity-sensitive shape memory with superior recovery stress. *Mater. Chem. Front.* **3**, 2472–2482 (2019).
61. Otkovs, M. et al. Degree of biomimicry of artificial spider silk spinning assessed by NMR spectroscopy. *Angew. Chem. Int. Ed.* **56**, 12571–12575 (2017).
62. Landreh, M., et al. Mass spectrometry captures structural intermediates in protein fiber self-assembly. *Chem. Commun.* **53**, 3319–3322 (2017).
63. Brown, C. P., Rosei, F., Traversa, E. & Licoccia, S. Spider silk as a load bearing biomaterial: tailoring mechanical properties via structural modifications. *Nanoscale* **3**, 870 (2011).
64. Sampath, S. & Yarger, J. L. Structural hysteresis in dragline spider silks induced by supercontraction: an X-ray fiber micro-diffraction study. *RSC Adv.* **5**, 1462–1473 (2015).
65. Yazawa, K., Malay, A. D., Masunaga, H. & Numata, K. Role of skin layers on mechanical properties and supercontraction of spider dragline silk fiber. *Macromol. Biosci.* **19**, 1–7 (2018).
66. Hu, L., Chen, Q., Yao, J., Shao, Z. & Chen, X. Structural changes in spider dragline silk after repeated supercontraction – Stretching processes. *Biomacromolecules* **21**, 5306–5314 (2020).
67. Grubb, D. T. & Ji, G. Molecular chain orientation in supercontracted and re-extended spider silk. *Int. J. Biol. Macromol.* **24**, 203–210 (1999).
68. Yarger, J. L., Cherry, B. R. & Van Der Vaart, A. Uncovering the structure-function relationship in spider silk. *Nat. Rev. Mater.* **3**, 18008 (2018).
69. Blamires, S. J., Blackledge, T. A. & Tso, I.-M. Physicochemical property variation in spider silk: ecology, evolution, and synthetic production. *Annu. Rev. Entomol.* **62**, 443–460 (2017).
70. Berg, J. M., Tymoczko, J. L. & Stryer, L. *Biochemistry*. (W H Freeman, 2002).
71. Lefranc, M.-P. & Lefranc, G. *The Immunoglobulin FactsBook*. (Academic Press, 2001).
72. Shao, Z. & Vollrath, F. The effect of solvents on the contraction and mechanical properties of spider silk. *Polymer*. **40**, 1799–1806 (1999).
73. Blackledge, T. A. et al. How super is supercontraction? Persistent versus cyclic responses to humidity in spider dragline silk. *J. Exp. Biol.* **212**, 1981–1989 (2009).
74. Greco, G., Pantano, M. F., Mazzolai, B. & Pugno, N. M. Imaging and mechanical characterization of different junctions in spider orb webs. *Sci. Rep.* **9**, 5776 (2019).
75. Blackledge, T. A., Cardullo, R. A. & Hayashi, C. Y. Polarized light microscopy, variability in spider silk diameters, and the mechanical characterization of spider silk. *Invertebr. Biol.* **124**, 165–173 (2005).
76. Swanson, B. O., Anderson, S. P., DiGiovine, C., Ross, R. N. & Dorsey, J. P. The evolution of complex biomaterial performance: the case of spider silk. *Integr. Comp. Biol.* **49**, 21–31 (2009).
77. Swanson, B. O., Blackledge, T. A., Beltrán, J. & Hayashi, C. Y. Variation in the material properties of spider dragline silk across species. *Appl. Phys. A Mater. Sci. Process.* **82**, 213–218 (2006).
78. Gosline, J. M., DeMont, M. E. & Denny, M. W. The structure and properties of spider silk. *Endeavour* **10**, 37–43 (1986).
79. Denny, M. The physical properties of spider's silk and their role in the design of orb-webs. *J. Exp. Biol.* **65**, 483–506 (1976).
80. Adachi, K. *Matrix-Based Introduction to Multivariate Data Analysis*. (Springer, 2020).
81. Guinea, G. V., Elices, M., Pérez-Rigueiro, J. & Plaza, G. Self-tightening of spider silk fibers induced by moisture. *Polymer*. **44**, 5785–5788 (2003).
82. Pérez-Rigueiro, J., Elices, M. & Guinea, G. V. Controlled supercontraction tailors the tensile behaviour of spider silk. *Polymer*. **44**, 3733–3736 (2003).
83. Gonska, N. et al. Structure-function relationship of artificial spider silk fibers produced by straining flow spinning. *Biomacromolecules* **21**, 2116–2124 (2020).
84. Baldassarre, M. et al. Simultaneous fitting absorption spectra and their second derivatives for an improved analysis of protein infrared spectra. *Molecules*. **20**, 12599–12622 (2015).

Acknowledgements

The authors would like to thank Marlene Andersson for providing the photo in Fig. 1b. The authors would like to thank Lorenzo Moschini, Prof. Antonella Motta, and Prof. Claudio Migliaresi (Biotech – Mattarello, University of Trento) for their support with SEM facility. N.M.P. is supported by the European Commission under the FET Proactive (“Neurofibers”) grant No. 732344 as well as by the Italian Ministry of Education, University and Research (MIUR) under the “Departments of Excellence” grant L. 232/2016, the ARS01-01384-PROSCAN and the PRIN-20177TTP3S grants. G.G. is supported by PRIN-20177TTP3S grant. FTIR spectrometer was funded by Knut och Alice Wallenbergs Stiftelse. A.R. has received funding from the European Research Council (ERC) under the European Union's Horizon 2020 research and innovation program (grant agreement No 815357), the Center for Innovative Medicine (CIMED) at Karolinska Institute and Stockholm City Council, Karolinska Institute SFO Regen (FOR 4-1364/2019), the Swedish Research Council (2019-01257), and Formas (2019-00427).

Author contributions

Conceptualization, G.G. and A.R.; methodology, G.G. and A.R.; validation, G.G., and A.R.; investigation, G.G., T.A., B.S., J.F., N.G., O.S., F.G.B., and G.S.; resources, A.R. and N.M.P.; data curation, G.G. and B.S.; writing—original draft preparation, G.G., T.A., B.S., and A.R.; writing—review and editing, G.G., T.A., B.S., J.F., O.S., A.B., G.S., V.K., J.J., A.R., and N.M.P.; supervision, N.M.P. and A.R.; project administration, A.R.; funding acquisition, A.R. and N.M.P. All authors have read and agreed to the published version of the manuscript.

Funding

Open access funding provided by Karolinska Institute.

Competing interests

The authors declare no competing interests.

Additional information

Supplementary information The online version contains supplementary material available at <https://doi.org/10.1038/s43246-021-00147-w>.

Correspondence and requests for materials should be addressed to N.M.P. or A.R.

Peer review information Primary handling editor: John Plummer.

Reprints and permission information is available at <http://www.nature.com/reprints>

Publisher's note Springer Nature remains neutral with regard to jurisdictional claims in published maps and institutional affiliations.



Open Access This article is licensed under a Creative Commons Attribution 4.0 International License, which permits use, sharing, adaptation, distribution and reproduction in any medium or format, as long as you give appropriate credit to the original author(s) and the source, provide a link to the Creative Commons license, and indicate if changes were made. The images or other third party material in this article are included in the article's Creative Commons license, unless indicated otherwise in a credit line to the material. If material is not included in the article's Creative Commons license and your intended use is not permitted by statutory regulation or exceeds the permitted use, you will need to obtain permission directly from the copyright holder. To view a copy of this license, visit <http://creativecommons.org/licenses/by/4.0/>.

© The Author(s) 2021

Supplementary information

Tyrosine residues mediate supercontraction in biomimetic spider silk

Gabriele Greco¹, Tina Arndt², Benjamin Schmuck², Juanita Francis², Fredrik G. Bäcklund², Olga Shilkova², Andreas Barth³, Nathalie Gonska⁴, Gulaim Seisenbaeva⁵, Vadim Kessler⁵, Jan Johansson², Nicola M. Pugno^{1,6,*} and Anna Rising^{2,4,*}

¹ Laboratory of Bio-Inspired, Bionic, Nano, Meta, Materials & Mechanics, Department of Civil, Environmental and Mechanical Engineering, University of Trento, Via Mesiano, 77, 38123 Trento, Italy

² Department of Biosciences and Nutrition, Karolinska Institutet, Neo, 14183 Huddinge, Sweden

³ Department of Biochemistry and Biophysics, The Arrhenius Laboratories for Natural Sciences, Stockholm University, 10691 Stockholm, Sweden

⁴ Department of Anatomy, Physiology and Biochemistry, Swedish University of Agricultural Sciences, 750 07 Uppsala, Sweden

⁵ Department of Chemistry and Biotechnology, Swedish University of Agricultural Sciences, 750 07 Uppsala, Sweden

⁶ School of Engineering and Materials Science, Queen Mary University of London, Mile End Road, London E1 4NS, UK

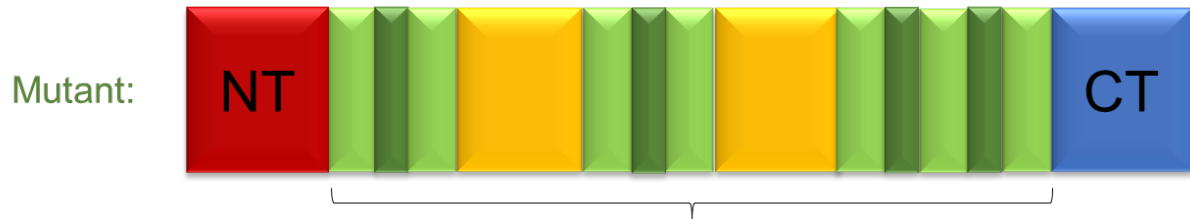
*Corresponding authors: nicola.pugno@unitn.it; anna.rising@ki.se

NT: SHTTPWTNPGLAENFMNSFMQGLSSMPGFTASQLDDMSTIA
 QSMVQSIQSLAAQGRTPNKLQALNMAFASSMAEIAASEEGG
 GSLSTKTSSIASAMSN AFLQTTGVVNQPFINEITQLVSMFAQA
 GMNDVSA

CT: TSGGYGYGTSAAAGAGVAAGSYAGAVNRLSSAEAA SRVSSNI
 AAIASGGASALPSVISNIYSGVVASGVSSNEALIQALLELLSALV
 HVLSSASIGNVSSVGV DSTLN VVQDSV GQYVG

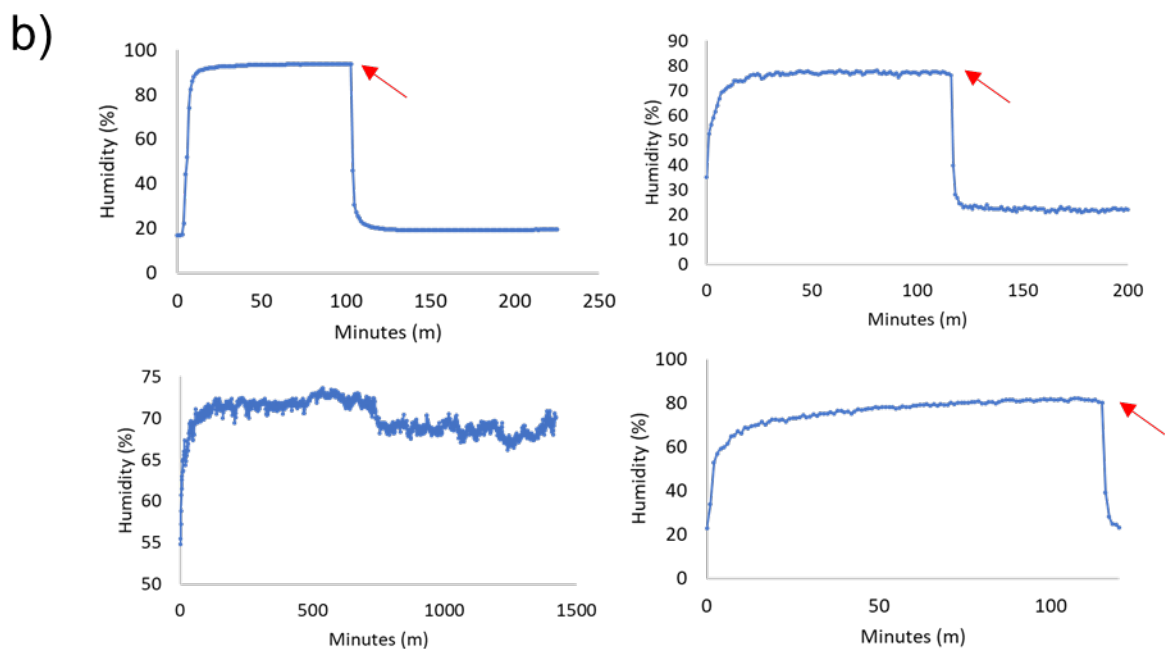
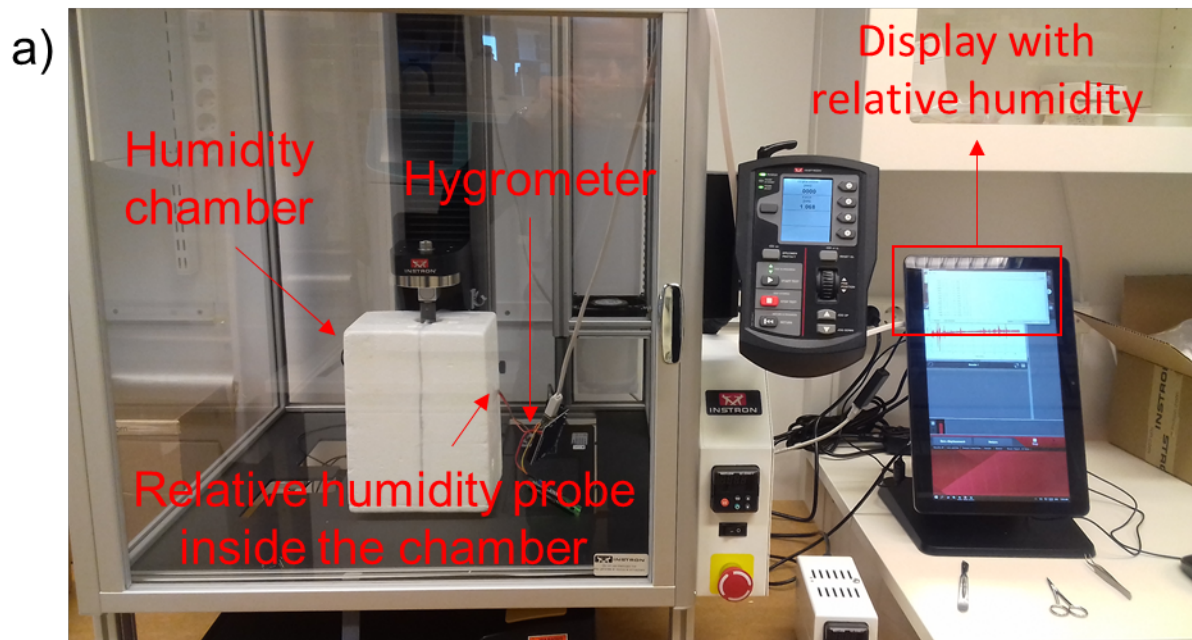


2Rep: GNSGRGQGGY GQGSGGNAAAAAAAAAAAAAAAAAGQGGQGGYGR
 QSQGAGSAAAAAAAAAAAAAAAAAGSGQGGYGGQGGQGGY GQSGNS

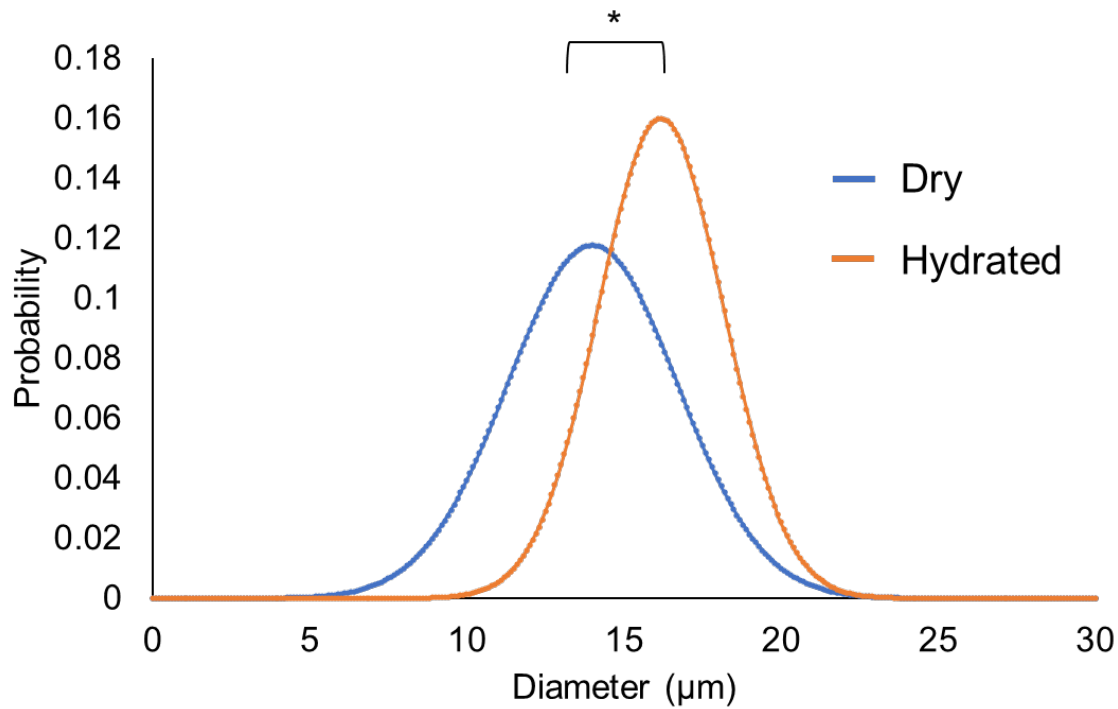


2Rep^{Y-F}: GNSGRGQGGF GQGSGGNAAAAAAAAAAAAAAAAAGQGGQGGFGR
 QSQGAGSAAAAAAAAAAAAAAAAAGSGQGGFGGQGGQGGF GQSGNS

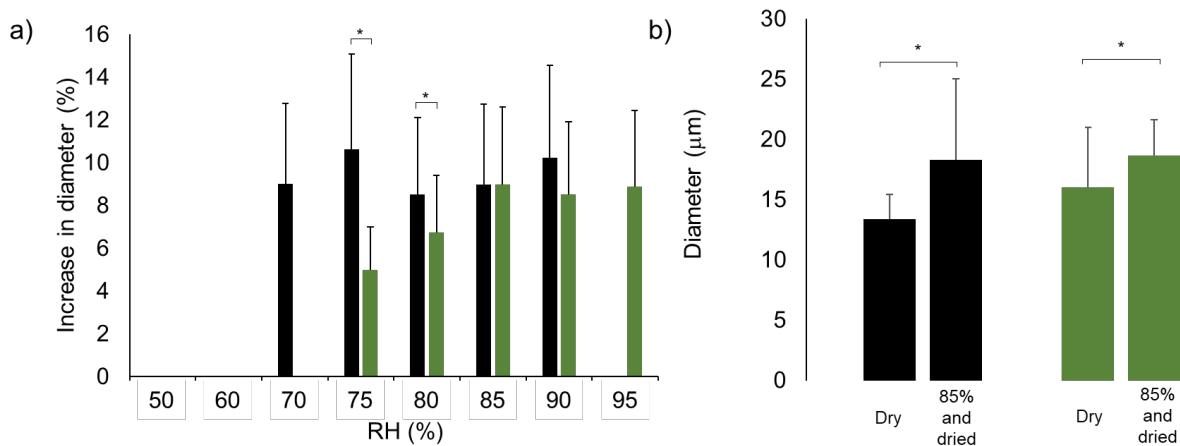
Supplementary Figure 1: NT2RepCT and NT2Rep^{Y-F}CT. Schematic presentation of the two designed spider silk proteins studied and primary structure of the NT2RepCT and NT2Rep^{Y-F}CT.



Supplementary Figure 2: Experimental set-up of tensile tester and stability of humidity chamber. a) Custom-made humidity chamber coupled with the tensile tester and the humidity sensor. b) The stability of the humidity in the chamber over time. The graphs show the different relative humidity (%) used in this study inside the chamber vs time (min). The red arrows indicate the timepoint when the chamber was opened (which led to a decrease in relative humidity).

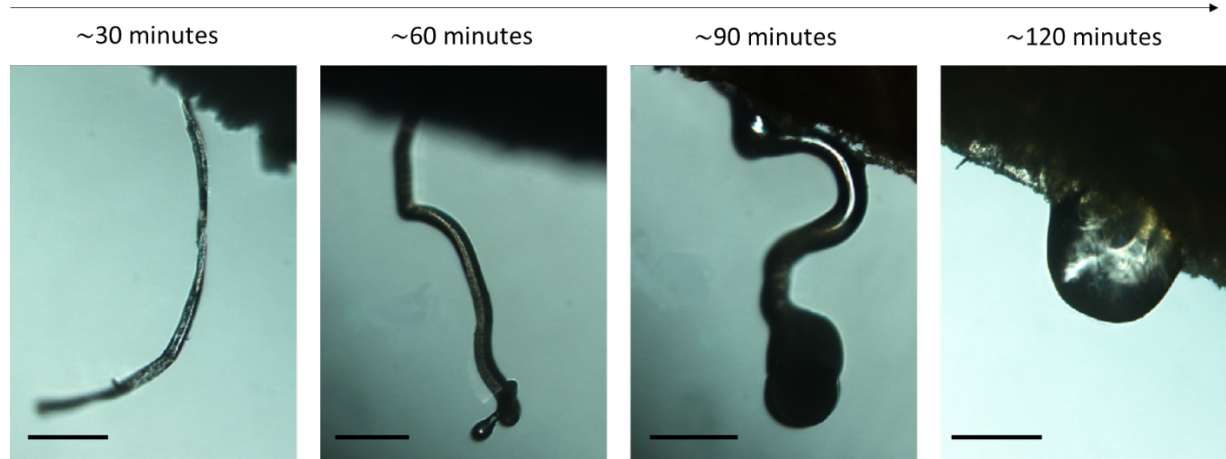


Supplementary Figure 3. Distribution of diameters of NT2RepCT fibers before and after hydration. An example of two distributions of the diameters before and after the hydration process (NT2RepCT fibers). Asterisks above the histograms indicate significant differences (p -value <0.05).

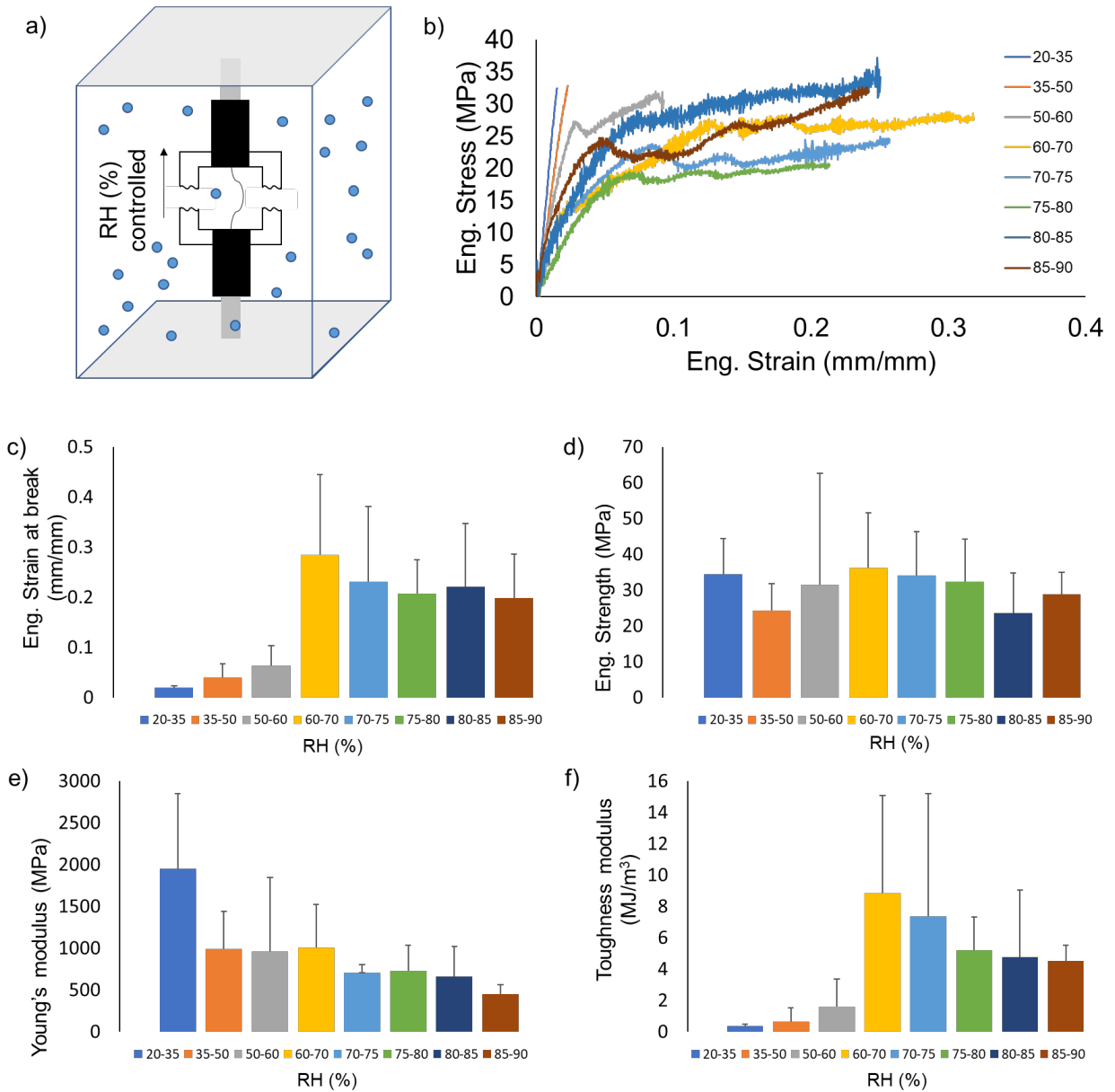


Supplementary Figure 4. Fiber diameters increase in response to increased humidity. a) Increase in diameter of the fibers kept at different humidity rates (RH). b) Diameter values of the fibers kept at 85% RH and then dried at 35% RH, compared with the dry ones (at 35%). Green is used for NT2Rep^{Y-FC}T and black for NT2RepCT. Asterisks above the histograms indicate significant differences (p -value <0.05). The error bars are the standard deviation of the data set.

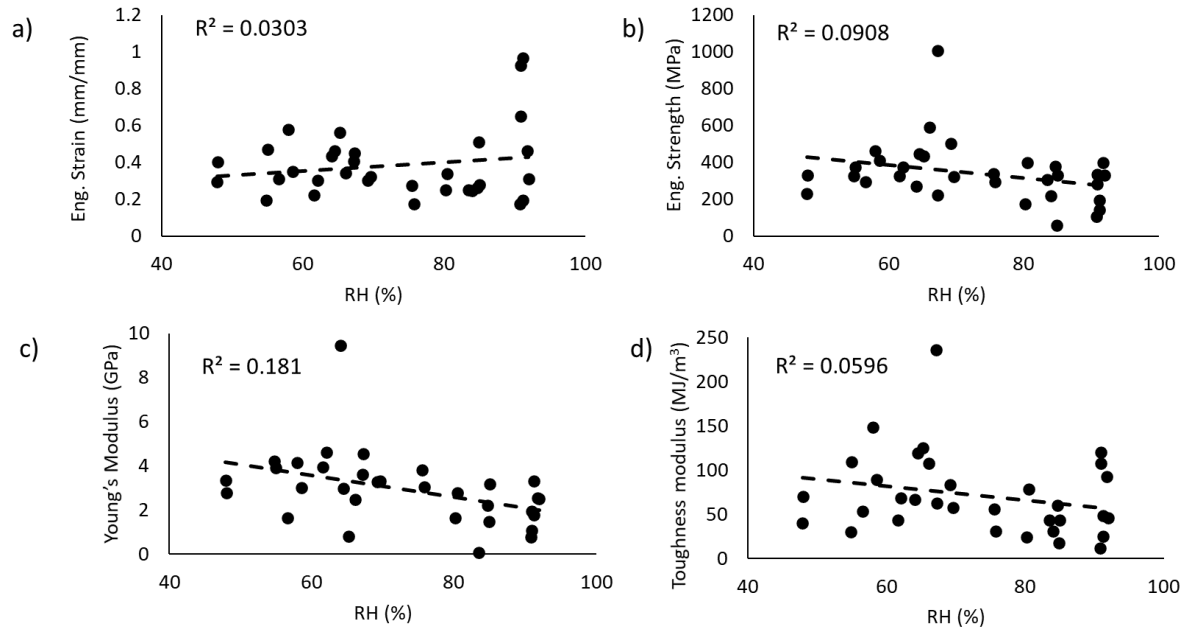
Time



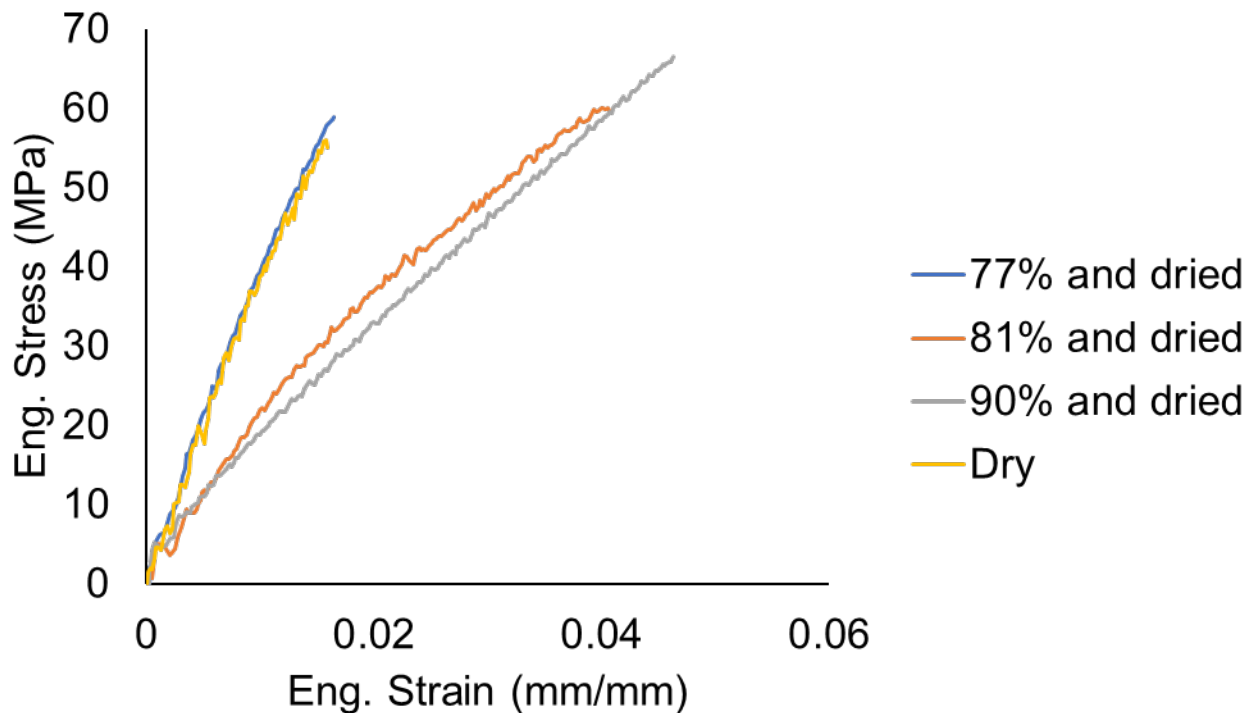
Supplementary Figure 5. Appearance of NT2RepCT fibers over time at 90% relative humidity. The pictures show the appearance of one individual NT2RepCT fiber at different time points (total incubation time 120 minutes). Scale bars: 100 μm .



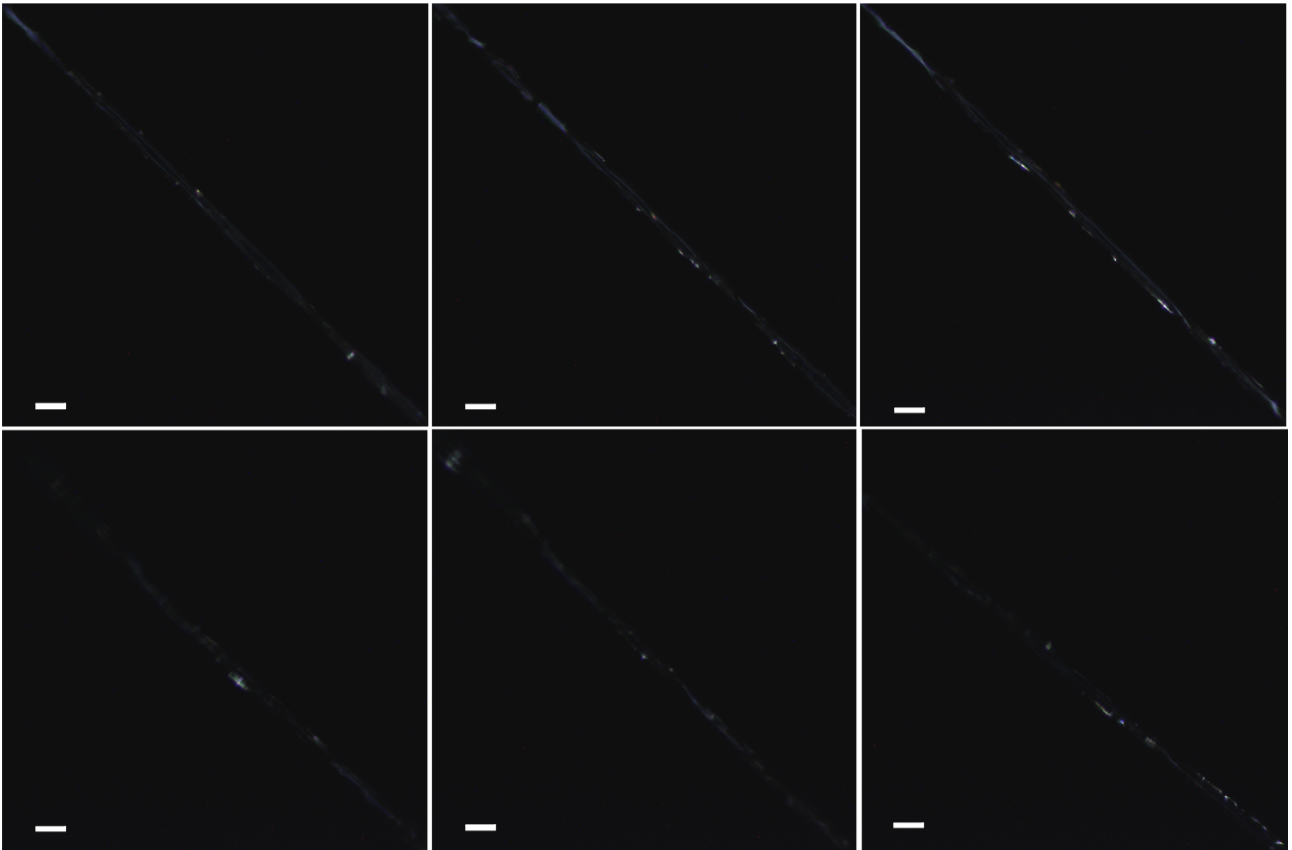
Supplementary Figure 6. Mechanical tests of NT2RepCT fibers at different relative humidities. : a) Schematic image of the setup in which the fibers were tested at different relative humidity (RH). b) Representative stress-strain curves of the NT2RepCT fibers tested at different RH and their mechanical properties: c) Eng. Strain at break, d) Eng. Strength, e) Young's modulus, and f) toughness modulus. The error bars are the standard deviation of the data set.



Supplementary Figure 7. Mechanical properties of native spider silk at different relative humidity. Mechanical properties vs relative humidity (RH) (%) for *Trichonephila clavipes* silk: a) Eng. Strain at break, b) Eng. Strength, c) Young's modulus, and d) toughness modulus.



Supplementary Figure 8: Representative stress-strain curves of NT2RepCT fibers. Samples were mounted restrained in both ends in the tensile tester in the humidity chamber and incubated for 60 minutes at a specific relative humidity as indicated in the graph. The fibers were then then dried (at 35% relative humidity) for 100 minutes before testing.



Supplementary Figure 9. Polarized microscopy images of NT2RepCT fibers. Images were captured before (upper row), and after (lower row) 2h incubation at 85% humidity. Scale bars equals 50 micrometers.



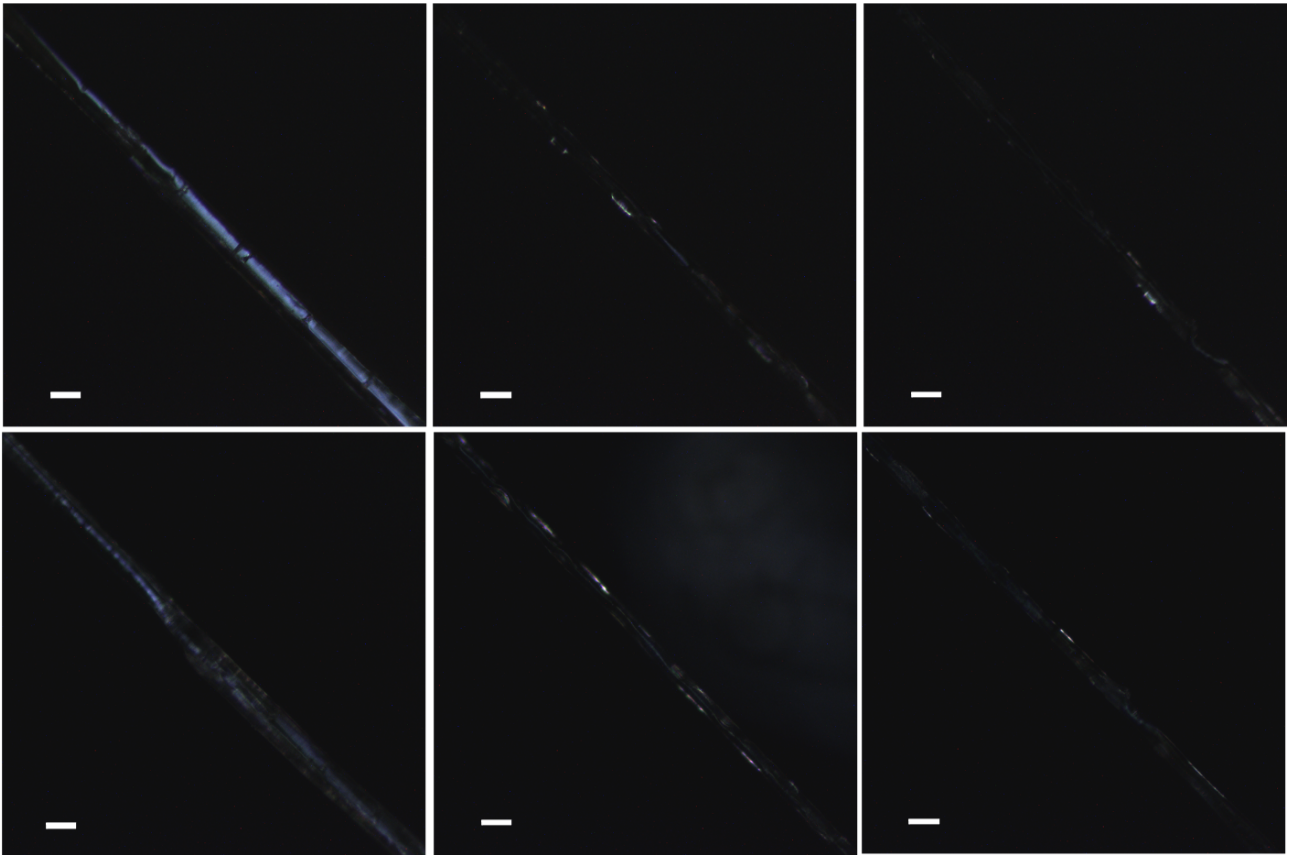
Supplementary Figure 10. Polarized microscopy images of NT2RepCT fibers. Images were captured before (upper row), and after (lower row) 2h incubation at 85% humidity. Scale bars equals 50 micrometers.



Supplementary figure 11. Polarized microscopy images of NT2RepCT fibers. Images were captured before (upper row), and after (lower row) 2h incubation at 85% humidity. Scale bars equals 50 micrometers.



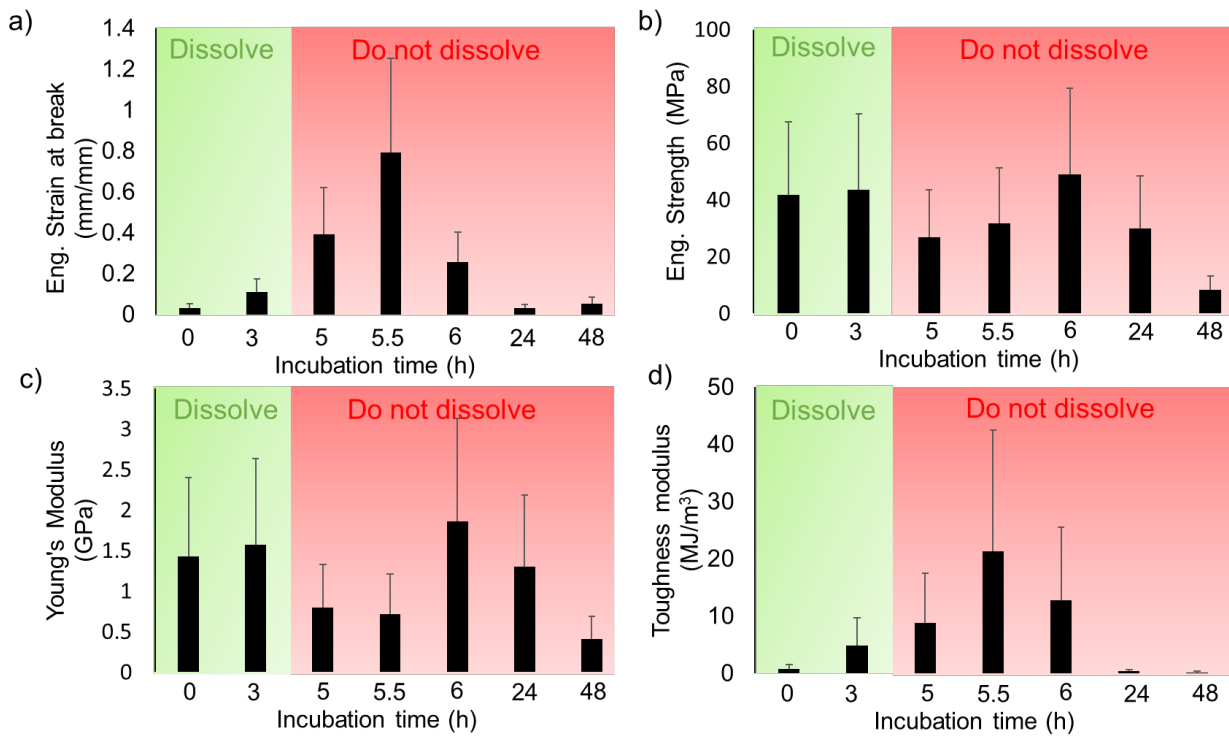
Supplementary Figure 12. Polarized microscopy images of NT2Rep^{Y-FCT} fibers. Images were captured before (upper row), and after (lower row) 2h incubation at 85% humidity. Scale bars equals 50 micrometers.



Supplementary Figure 13. Polarized microscopy images of NT2Rep^{Y-FC}T fibers. Images were captured before (upper row), and after (lower row) 2h incubation at 85% humidity. Scale bars equals 50 micrometers.



Supplementary Figure 14. Polarized microscopy images of NT2Rep^{Y-FC}T fibers. Images were captured before (upper row), and after (lower row) 2h incubation at 85% humidity. Scale bars equals 50 micrometers.



Supplementary Figure 15: Prolonged incubation in the spinning bath affects fiber mechanical properties and makes fibers resistant to dissolution. The effect of prolonged spinning bath incubation on the mechanical properties of the NT2Rep^{Y-FCT} fibers. After 5 h the fibers did not dissolve in dH₂O or PBS, respectively. For corresponding values for the NT2RepCT fibers, see Greco et al.⁴⁶. The error bars are the standard deviation of the data set.

Supplementary Table 1: Values of the contraction in length and increase in diameter of the NT2RepCT and NT2Rep^{Y-FCT} tested.

Relative humidity (%)	Sample	Nr samples	Contraction in length (%)	Increase in diameter (%)
70	NT2RepCT	10	6.4 ± 3.5	9.0 ± 5.8
	NT2Rep ^{Y-FCT}	10	4.0 ± 2.7	Not detected
75	NT2RepCT	10	21.3 ± 6.5	10.6 ± 6.0
	NT2Rep ^{Y-FCT}	10	5.5 ± 3.1	5 ± 2.6
80	NT2RepCT	10	16.8 ± 9.6	8.5 ± 4.6
	NT2Rep ^{Y-FCT}	10	10.7 ± 5.1	6.7 ± 3.3
85	NT2RepCT	10	24.7 ± 11.5	9.0 ± 3.9
	NT2Rep ^{Y-FCT}	10	20.2 ± 13.1	9.0 ± 5.0
90	NT2RepCT	10	40.6 ± 10.6	10.2 ± 2.3
	NT2Rep ^{Y-FCT}	10	21.9 ± 12.5	8.5 ± 4.1
95	NT2RepCT	10	Dissolved	Dissolved
	NT2Rep ^{Y-FCT}	10	34.5 ± 7	8.9 ± 3.7

Supplementary Table 2: Pairwise comparison of the contraction in length (and increase in diameter) between NT2RepCT and NT2Rep^{Y-F}CT at different relative humidity. Black boxes indicate that the p-value was higher than 0.05.

Pairwise comparison of the contraction in length	
Relative humidity (%)	P-value
70	0.0150
75	0.0001
80	0.0270
85	
90	0.0110
95	
Pairwise comparison of the increase in diameter	
Relative Humidity (%)	P-value
70	
75	0.003
80	0.048
85	
90	
95	

Supplementary Table 3: Mechanical properties of the fibers as spun or supercontracted at 85% relative humidity (RH) with an unrestrained end and then dried again.

Sample	Nr. Fibers	Diameter (mm)	Eng. Strain at break (mm/mm)	Eng. Strength (MPa)	Young's modulus (GPa)	Toughness modulus (MJ/m ³)
NT2RepCT (dry)	17	15 ± 2	0.02 ± 0.01	34 ± 10	2.0 ± 0.9	0.35 ± 0.12
NT2RepCT (freshly spun)	16	20 ± 5	0.03 ± 0.01	36 ± 18	1.5 ± 0.8	0.63 ± 0.39
NT2Rep ^{Y-F} CT Dry	17	16 ± 5	0.03 ± 0.01	42 ± 23	1.4 ± 0.8	0.77 ± 0.54
NT2RepCT (dried after RH 85%)	9	18 ± 7	0.03 ± 0.01	26 ± 13	0.9 ± 0.6	0.40 ± 0.24
NT2Rep ^{Y-F} CT (dried after RH 85%)	13	19 ± 3	0.02 ± 0.02	22 ± 16	1.6 ± 1.1	0.29 ± 0.34

Supplementary Table 4: Pairwise comparison p-values of the properties of the dry fibers (both NT2RepCT and NT2Rep^{Y-F}CT) and those of the same fibers exposed at 85% relative humidity (RH) and then dried. Black boxes indicate that the p-value was higher than 0.05.

Pairwise comparison between dry and exposed at 85% RH and then dried		P-value
Diameter	NT2RepCT	0.011
	NT2Rep ^{Y-F} CT	0.048
Eng. Strain at break	NT2RepCT	
	NT2Rep ^{Y-F} CT	0.045
Eng. Strength	NT2RepCT	0.002

	NT2Rep ^{Y-FCT}	0.038
Young's modulus	NT2RepCT	0.008
	NT2Rep ^{Y-FCT}	
Toughness modulus	NT2RepCT	0.026
	NT2Rep ^{Y-FCT}	0.049

Supplementary Table 5: MANOVA analysis of the mechanical properties of NT2RepCT and NT2Rep^{Y-FCT} fibers that were tested in the dry state before supercontraction and after being supercontracted at 85% relative humidity (RH) and then dried. The table shows the maximal estimated dimension and the p-values for each dimension. If d=0 the means are all the same, if d=1 the means fall on a line, and if d=2 the means fall on a plane.

Type of fiber	Comparison	Dimension (d)	p-values
NT2RepCT	Dry vs supercontracted at 85% RH and dried	1	0.007 (for d=0)
NT2Rep ^{Y-FCT}	Dry vs supercontracted at 85% RH and dried	1	0.012 (for d=0)

Supplementary Table 6: Relative secondary structure content of the NT2RepCT and NT2Rep^{Y-FCT}, when the fiber was as spun (dried state) or after being supercontracted at 85% relative humidity (RH).

	NT2RepCT dry, as spun	NT2RepCT dry, supercontracted at 85% RH	NT2Rep ^{Y-FCT} dry, as spun	NT2Rep ^{Y-FCT} dry, supercontracted at 85% RH
β - sheet (%)	40.3 \pm 4.1	40.2 \pm 4.4	45.0 \pm 7.5	47.2 \pm 4.4
α -helix/disordered (%)	28.7 \pm 1.4	26.8 \pm 10.8	27.9 \pm 7.1	27.5 \pm 4.0
turns (%)	17.3 \pm 2.9	15.4 \pm 8.0	17.7 \pm 5.3	14.0 \pm 3.6

The average and standard deviation were obtained from differently smoothed spectra using a Savitzky–Golay window of 13, 15, 17, and 19 points.

Supplementary Table 7: Width at half maximal absorbance in the amide region I (1600 – 1700 cm⁻¹)

	Width at half maximal absorbance (cm ⁻¹)
NT2RepCT dry, as spun	61.5 \pm 3.0
NT2RepCT dry supercontracted at 85% RH	65.2 \pm 2.1
NT2Rep ^{Y-FCT} dry, as spun	64.5 \pm 2.2
NT2Rep ^{Y-FCT} dry supercontracted at 85% RH	69.2 \pm 2.3